

The SRG/eROSITA All-Sky Survey

Subaru/HSC-SSP weak-lensing mass measurements for the eRASS1 Galaxy Clusters

Nobuhiro Okabe^{1,2,3}, Thomas Reiprich⁴, Sebastian Grandis⁵, I-Non Chiu⁶, Masamune Oguri^{7,8}, Keiichi Umetsu⁶, Esra Bulbul⁹, Emre Bahar⁹, Fabian Balzer⁹, Nicolas Clerc¹⁰, Johan Comparat⁹, Vittorio Ghirardini⁹, Florian Kleinebreil⁵, Matthias Kluge⁹, Ang Liu^{9,11}, Yen-Ting Lin⁶, Rogério Monteiro-Oliveira⁶, Florian Pacaud⁴, Miriam Ramos Ceja⁹, Jeremy Sanders⁹, Tim Schrabback⁵, Riccardo Seppi⁹, Martin Sommer⁴, and Xiaoyuan Zhang⁹

Affiliations at the end of the paper, e-mail: okabe@hiroshima-u.ac.jp

ABSTRACT

We perform individual weak-lensing (WL) mass measurements for 78 eROSITA's first All-Sky Survey (eRASS1) clusters in the footprint of Hyper Suprime-Cam Subaru Strategic Program (HSC-SSP) S19A, without any priors of the eRASS1 X-ray quantities or assumption of the mass and concentration relation. In the sample, we find 3 clusters are mis-associated with optical counterparts and 12 clusters are poorly fitted with an NFW profile. The average mass for the 12 poor-fit clusters changes from $\sim 10^{14} h_{70}^{-1} M_{\odot}$ to $\sim 2 \times 10^{13} h_{70}^{-1} M_{\odot}$ when lensing contamination from surrounding mass structures is taken into account. The scaling relations between the true mass and cluster richness and X-ray count-rate agree well with the results of the eRASS1 Western Galactic Hemisphere region based on count-rate-inferred masses, which are calibrated with the HSC-SSP, DES, and KiDS surveys. We develop a Bayesian framework for inferring the mass-concentration relation of the cluster sample, explicitly incorporating the effects of weak-lensing mass calibration in the mass-concentration parameter space. The redshift-dependent mass and concentration relation is in excellent agreement with predictions of dark-matter-only numerical simulations and previous studies using X-ray-selected clusters. Based on the two-dimensional (2D) WL analysis, the offsets between the WL-determined centers and the X-ray centroids for 36 eRASS1 clusters with high WL S/N are described by two Gaussian components. We find that the mis-centering effect with X-ray centroids is smaller than that with peaks in the galaxy maps. Stacked mass maps support a small mis-centering effect even for clusters with low WL S/N. The projected halo ellipticity is $\langle \varepsilon \rangle = 0.45$ at $M_{200} \sim 4 \times 10^{14} h_{70}^{-1} M_{\odot}$, in agreement with results of numerical simulations and previous studies of clusters more than twice our mass.

Key words. Surveys - Galaxies: clusters: general - Galaxies: clusters: intracluster medium - X-rays: galaxies: clusters - Gravitational lensing: weak

1. Introduction

The evolution of the cluster mass function provides powerful constraints on cosmological parameters, especially the energy density of the total matter, the normalization of density fluctuation, and the dark energy (e.g. Chiu et al. 2023; Ghirardini et al. 2024; Artis et al. 2024a,b). Since the X-ray emissivity of thermal bremsstrahlung is proportional to the square of the electron number density, X-ray observations, which are less sensitive to projection effects, are a powerful tool for searching for galaxy clusters. The eROSITA (extended ROentgen Survey with an Imaging Telescope Array; Merloni et al. 2012; Predehl et al. 2021), on board the Spectrum Roentgen Gamma (SRG) mission (Sunyaev et al. 2021), is the unique instrument to discover an order of 10^5 galaxy clusters. Indeed, the eROSITA Final Equatorial Depth Survey (eFEDS) in a footprint with an area of $\sim 140 \text{ deg}^2$, significantly overlapping the Subaru/HSC-SSP footprint (Aihara et al. 2018, 2022), found 542 cluster candidates (Liu et al. 2022) and confirmed an optical counterpart of 477 clusters and groups (Klein et al. 2022). Recently, the eRASS1 (the Western Galactic Hemisphere of the eROSITA's first All-Sky Survey; Bulbul et al. 2024; Kluge et al. 2024) discovered 12,247 optically confirmed galaxy groups and clusters detected in the 0.2-2.3 keV over 13,116 deg^2 and constructed a sample for cosmology (Bul-

bul et al. 2024) with a high purity level of $\sim 95\%$, comprising 5259 optically confirmed clusters over an area of 12,791 deg^2 .

Accurate mass measurements of galaxy clusters are vitally important for cluster cosmology. Thanks to deep and wide optical surveys of ground-based telescopes of Subaru/HSC-SSP, DES, and KiDS (Chiu et al. 2022; Chiu et al. 2025; Grandis et al. 2024; Kleinebreil et al. 2024), the weak gravitational lensing effect can measure mass structures without assumptions of dynamical states. The weak-lensing (WL) mass measurements for eROSITA adopt the hierarchical Bayesian method to simultaneously fit the tangential shear profiles taking into account the relationship between mass and the count-rate for individual clusters (Chiu et al. 2022; Grandis et al. 2024; Chiu et al. 2025). The resulting WL mass is, therefore, a kind of count-rate-related mass. The adopted mass model assumes the mass and concentration relation for a Navarro-Frenk-White (NFW) model (Navarro et al. 1996, 1997), statistically treats a mis-centering effect by convolving a probability function, and uses the relationship between the true and WL masses based on numerical simulations.

In contrast, individual cluster lensing analysis enables us to simultaneously measure the two parameters, mass, and concentration, though it requires a large number of background galaxies (e.g. Okabe & Smith 2016; Umetsu et al. 2020). Furthermore,

two-dimensional WL analysis (Oguri et al. 2010) enables us to measure central positions for the assumed mass models, which assesses the mis-centering effect utilized in the statistical WL mass measurement. The lensing information also independently provides us with the purity of the detected clusters. Therefore, individual cluster lensing measurement is complementary to statistical cluster lensing analysis.

Thanks to the deep imaging of the Subaru/HSC-SSP, we perform cluster mass measurements for the eRASS1 clusters to understand and control WL systematics. The paper is organized as follows. We describe the WL mass measurement techniques in Sec 2, results in Sec 3, discussion in Sec 4, and conclusion in Sec. 5, respectively. Throughout the paper, we use $\Omega_{m,0} = 0.3$, $\Omega_{\Lambda,0} = 0.7$, and $H_0 = 70h_{70} \text{ kms}^{-1}\text{Mpc}^{-1} = 100h \text{ kms}^{-1}\text{Mpc}^{-1}$ with $h_{70} = 1$ and $h = 0.7$.

2. Weak-lensing analysis

We selected 78 clusters (Table 1 and Figure 1) for weak-lensing mass measurements from the 103 eRASS1 clusters in the HSC-SSP S19A footprint, according to the following criteria; the area fraction within $r < 3 h_{70}^{-1}\text{Mpc}$ centering the eRASS1 primary clusters (Ghirardini et al. 2024), where an HSC-3Y shape catalogue (see details in Li et al. 2022) is available, is greater than 70% and the innermost radius is less than $0.7 h_{70}^{-1}\text{Mpc}$. For instance, 23 clusters are removed because they are located around the edge of the HSC-Y3 footprint, so the galaxies in the shape catalogue are not distributed in all directions but only on one side or small patch region. The remaining 2 clusters are unavailable due to star masks in their central regions.

2.1. Background selection

The HSC-Y3 shape catalogue uses a method of Point Spread Function (PSF) correction known as re-Gaussianization (Hirata & Seljak 2003), which is implemented in the HSC pipeline (see details in Mandelbaum et al. 2018; Li et al. 2022). In weak-lensing mass measurements, we use only galaxies satisfying with the full-colour and full-depth condition from the HSC galaxy catalogue to achieve both precise shape measurement and photometric redshift estimation. We select background galaxies behind each cluster with the condition (Medezinski et al. 2018)

$$\int_{z_l+0.1} P(z) dz > 0.98, \quad (1)$$

where $P(z)$ is the probability of the photometric redshift from the machine learning method (MLZ; Carrasco Kind & Brunner 2014) calibrated with spectroscopic data (Tanaka et al. 2018; Nishizawa et al. 2020) and z_l is a cluster redshift. After background selection, the number density of background galaxies has a strong redshift dependence, varying from ~ 2 to ~ 12 [arcmin $^{-2}$], with an average of 7.0 ± 2.5 [arcmin $^{-2}$] (Figures 2 and B.1).

2.2. Mass estimation

The reduced tangential shear $\Delta\Sigma_+$ is computed by azimuthally averaging the measured tangential ellipticity, e_+ , for i -th galaxy in a given k -th annulus,

$$\Delta\Sigma_+(r_k) = \frac{\sum_i e_{+,i} w_i \langle \Sigma_{\text{cr}}(z_l, z_{s,i})^{-1} \rangle^{-1}}{2\mathcal{R}_k(1 + K_k) \sum_i w_i}, \quad (2)$$

where e_+ is the tangential ellipticity ($e_+ = -(e_1 \cos 2\varphi + e_2 \sin 2\varphi)$), w_i is the weighting function, $\langle \Sigma_{\text{cr}}(z_l, z_{s,i})^{-1} \rangle$ is the inverse of the mean critical surface mass density, \mathcal{R} is the shear responsivity, and K is the calibration factor. The weighting function is given by

$$w_i = \frac{1}{e_{\text{rms},i}^2 + \sigma_{e,i}^2} \langle \Sigma_{\text{cr}}(z_l, z_{s,i})^{-1} \rangle^2. \quad (3)$$

where e_{rms} and σ_e are the root mean square of intrinsic ellipticity and the measurement error per component ($\alpha = 1$ or 2), respectively. The inverse of the mean critical surface mass density is computed by the probability function $P(z)$, as follows,

$$\langle \Sigma_{\text{cr}}(z_l, z_{s,i})^{-1} \rangle = \frac{\int_{z_l}^{\infty} \Sigma_{\text{cr}}^{-1}(z_l, z_{s,i}) P(z_{s,i}) dz_{s,i}}{\int_0^{\infty} P(z_{s,i}) dz_{s,i}}. \quad (4)$$

Here, z_l and $z_{s,i}$ are the cluster and source redshift, respectively. The critical surface mass density is $\Sigma_{\text{cr}} = c^2 D_s / 4\pi G D_l D_{ls}$, where D_s and D_{ls} are the angular diameter distances from the observer to the sources and from the lens to the sources, respectively. The shear responsivity is expressed as

$$\mathcal{R} = 1 - \frac{\sum_i e_{\text{rms},i}^2 w_i}{\sum_i w_i}, \quad (5)$$

(see also Mandelbaum et al. 2005; Reyes et al. 2012). The measured values are corrected by the shear calibration factor (m, c) for individual objects (Li et al. 2022), where m is a multiplicative calibration bias and c an additive residual shear offset in the relation between the input and output shear component, $\gamma_{\text{output},\alpha} = (1 + m_\alpha)\gamma_{\text{input},\alpha} + c_\alpha$, as defined by STEP (Shear TESting Programme) simulations (Heymans et al. 2006; Massey et al. 2007). The calibration factor, K , is computed by

$$K = \frac{\sum_i m_i w_i}{\sum_i w_i}. \quad (6)$$

where m_i for individual galaxies are estimated based on GREAT3-like simulations (Mandelbaum et al. 2017, 2014, 2015) as a part of the GREAT (GRavitational lEnsing Accuracy Testing) project. We then subtract

$$\tilde{c} = \frac{\sum_i c_{+,i} w_i \langle \Sigma_{\text{cr},i}^{-1} \rangle^{-1}}{(1 + K) \sum_n w_n} \quad (7)$$

from $\langle \Delta\Sigma_+ \rangle(r_i)$ (equation 2). The additional offset term is negligible $\mathcal{O}(< 10^{-4})$ compared to $\langle \Delta\Sigma_+ \rangle \sim \mathcal{O}(10^{-1})$. The effective radius to describe the tangential shear at each annulus is shifted from the intermediate radius because the galaxy distribution of galaxies is partially missing because of the star mask. We thus adopt the weighted harmonic mean as the radius positions,

$$r_k = \frac{\sum_i w_i}{\sum_i r_i^{-1} w_i}, \quad (8)$$

which well explains a power-law tangential shear profile (Okabe & Smith 2016).

We use an NFW profile (Navarro et al. 1996) for the fitting of the model. The NFW mass density profile is described as

$$\rho_{\text{NFW}}(r) = \frac{\rho_s}{(r/r_s)(1 + r/r_s)^2}, \quad (9)$$

where ρ_s is the central density parameter and r_s is the scale radius. We use two parameters of the spherical mass, M_Δ , and the

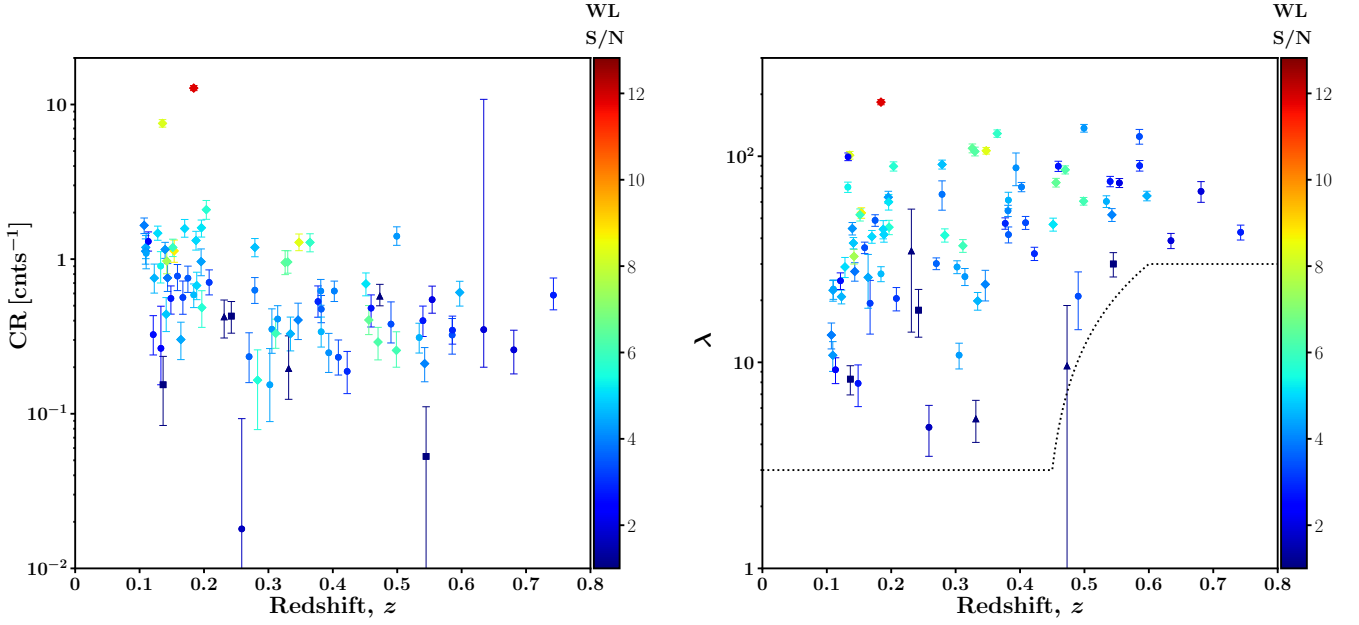


Fig. 1. Left: count-rate (CR) versus redshift (z). Right: richness (λ) versus redshift (z). The dotted line is the threshold described by a function connecting two constants with a linear function. Colours in all the panels denote the signal-to-noise ratio (S/N) of the reduced tangential shear profile. The circles, diamonds, squares, and up-triangles denote the clusters with 1D WL analysis only, 1D and 2D WL analysis, non-WL analysis, and mis-association, respectively.

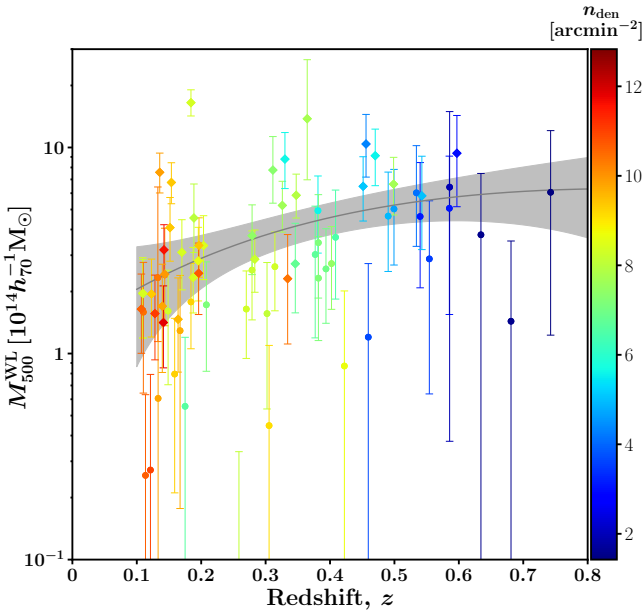


Fig. 2. weak-lensing masses ($M_{500}^{\text{WL}} [10^{14} h_{70}^{-1} M_{\odot}]$) versus redshift. The symbols are the same as in Figure 1. Colours denote the background number density, $n_{\text{den}} [\text{arcmin}^{-2}]$. The gray solid line and regions are the mean and 1σ region for the WL mass distribution in the parent sample obtained by the multivariate scaling relation analysis (Sec. 3.4), respectively.

halo concentration, c_{Δ} , instead of ρ_s and r_s . The spherical mass

and the halo concentration are defined by

$$M_{\Delta} = \frac{4}{3}\pi\Delta\rho_{\text{cr}}r_{\Delta}^3 \quad c_{\Delta} = \frac{r_{\Delta}}{r_s}, \quad (10)$$

respectively. Here, $\rho_{\text{cr}}(z)$ is the critical mass density at the cluster redshift and Δ is the overdensity. The reduced shear model, f_{model} , is described using the differential surface mass density $\Delta\tilde{\Sigma}_+$ and the local surface mass density Σ as follows,

$$f_{\text{model}} = \frac{\Delta\tilde{\Sigma}_+}{1 - \mathcal{L}_z\Sigma}, \quad (11)$$

where $\mathcal{L}_z = \sum_i (\Sigma_{\text{cr},i}^{-1})w_i / \sum_i w_i$. The log-likelihood is expressed as

$$-2 \ln \mathcal{L} = \ln(\det(C_{nm})) + \sum_{n,m} (\Delta\Sigma_{+,n} - f_{\text{model}}(r_n))C_{nm}^{-1}(\Delta\Sigma_{+,m} - f_{\text{model}}(r_m)), \quad (12)$$

where the covariance matrix, C , is composed of the uncorrelated large-scale structure (LSS), C_{LSS} , along the line-of-sight (Schneider et al. 1998), the shape noise C_g , and the error of photometric redshift C_s . We adopt maximum likelihood estimation (MLE).

When we compute the reduced tangential shear from a small number of background galaxies, internal substructures or surrounding clusters might accidentally affect mass measurements. Then we adopt the adaptive choice of binning scheme. We first fit 270 radial combinations of the innermost radii $r_{\text{in}} = [0.1 - 0.2] h_{70}^{-1} \text{Mpc}$ stepped by $0.05 h_{70}^{-1} \text{Mpc}$, the outermost radii $r_{\text{out}} = [2 - 3.6] h_{70}^{-1} \text{Mpc}$ stepped by $0.2 h_{70}^{-1} \text{Mpc}$, and the number of bins $N_{\text{bin}} = [4 - 8]$ stepped by 1. Then, we compute average masses within the overdensities of $\Delta = 2500, 100, 500, 200$, and vir and choose a radial bin set closest to the average values. If the innermost galaxy is farther away than r_{in} , the first radius of r_{in} is

taken as its position without changing the annulus width. To minimize lensing contamination from the nearest clusters in the reduced tangential shear profile, we compute the distance between the target cluster and the nearest one from the eRASS1 cluster catalogue. If the distance between the two clusters is closer than the outermost radius, the largest radius of r_{out} is taken as half the distance. We stress that we do not use any external catalogues to search for the neighbouring clusters for the purpose of mass measurements in a self-consistent manner.

2.3. Weak-lensing mass reconstruction

After background selection, we pixelize the shear distortion data in a regular grid of pixels using a Gaussian kernel $G \propto \exp[-\theta^2/(2\sigma_g^2)]$ with FWHM = $2\sqrt{2\ln 2}\sigma_g$. In the mass reconstruction, we assume the weak-lensing limit: $\Delta\Sigma_\alpha \simeq \Delta\tilde{\Sigma}_\alpha$ where $\alpha = 1, 2$. The dimensional shear field at angular position θ is obtained by

$$\Delta\tilde{\Sigma}_\alpha(\theta) = \frac{\sum_i e_{\alpha,i} G(\theta_i - \theta) w_i \langle \Sigma_{\text{cr}}(z_l, z_{s,i})^{-1} \rangle^{-1}}{2\tilde{\mathcal{R}}(1 + \tilde{K}) \sum_i G(\theta_i - \theta) w_i}, \quad (13)$$

where $\tilde{\mathcal{R}}$ and \tilde{K} are computed with a lensing weight added by the Gaussian kernel, that is, w_i is replaced by $w_i G(\theta_i - \theta)$ in the equations (5 and 6). Since the above Gaussian smoothing is the convolution integral, we perform it in the Fourier space at the same time as the Kaiser & Squires inversion method (Kaiser & Squires 1993) to invert the pixelized shear field to the mass map. If there are blank areas due to the bright star mask in a map-making field, we fill in dummy data in the region and mask it after the mass reconstruction. The spatial positions of the dummy are generated from a random uniform distribution. The shape and photo- z data of the dummy are taken randomly from the real data, and the ellipticities are then randomly rotated. We estimate the mass reconstruction errors by the bootstrapping method. We fix the positions of background galaxies and randomly rotate an ellipticity component taken from other galaxies. This is repeated for 500 realizations, and the error is estimated as the standard error of the mock mass maps. The S/N for the mass map is obtained by dividing the reconstructed mass maps by the noise maps. We adopt FWHM=400 h_{70}^{-1} kpc and 1' for the individual and stacked map making, respectively.

2.4. Two-dimensional analysis

The mass modeling using the two-dimensional shear pattern enables us to parameterize cluster central positions as well as cluster masses (Oguri et al. 2010). The mis-centering effect is one of the important parameters for the simultaneous analysis of ensemble samples of clusters (Chiu et al. 2022; Chiu et al. 2025; Grandis et al. 2024). For this purpose, we compute the shear grids every 1.5 arcmin in the square box of half-size $3 h_{70}^{-1}$ Mpc, centering the eRASS1 positions. The ensemble averages of the ellipticity components and positions are calculated similarly to the eqs. 2 and 8, respectively. The log-likelihood is expressed as

$$-2 \ln \mathcal{L} = \ln(\det(C_{\alpha\beta, nm})) + \sum_{\alpha, \beta=1}^2 \sum_{n, m} (\Delta\Sigma_{\alpha, n} - f_{\text{model}, \alpha}(r_n)) C_{\alpha\beta, nm}^{-1} (\Delta\Sigma_{\alpha, m} - f_{\text{model}, \beta}(r_m)), \quad (14)$$

where the indices α and β are the two components of shear distortion. We consider shape noise only in the covariance matrix

to reduce the computation time. The parameters are the parameters of the mass models and their centers. We use three types of mass models: the spherical NFW model, an elliptical NFW mass model, and multi-components of the spherical mass model. The spherical NFW model is the same as that used in the one-dimensional analysis.

The elliptical NFW model (see also Oguri 2021, for fast computation) takes into account the ellipticity of the mass distribution on the sky plane (Oguri et al. 2010). The two-dimensional halo ellipticity, ε , is defined by $1 - b/a$, where a and b are the major and minor axes of the mass distribution on the sky plane, respectively. The distance of an iso-contours from the centers is obtained by

$$\begin{aligned} r &= (x'^2/(1 - \varepsilon) + (1 - \varepsilon)y'^2)^{1/2}, \\ x' &= x \cos \phi_e + y \sin \phi_e, \\ y' &= -x \sin \phi_e + y \cos \phi_e. \end{aligned} \quad (15)$$

Here, ϕ_e is an orientation angle of the major axis measured from the north to the east.

If there are multiple clusters in the data field, the center of a single NFW model might be affected. In this case, we consider the multi-component spherical NFW model. If the mass map has a peak of more than 4σ , which is FWHM away from the eRASS1 centroids, we add mass components other than the target clusters at its peak-finding position to investigate how much the WL-determined central positions are changed. We assume the mass-concentration relation (Diemer & Kravtsov 2015) for non-target clusters.

We use the Markov chain Monte Carlo (MCMC) method and treat the logarithmic quantities for M_{200} and c_{200} as parameters because they are positive. We use flat priors for all the parameters; $|\text{R.A.} - \text{R.A.}_{\text{eRASS1}}| < 3 [h_{70}^{-1} \text{Mpc}]/D_l$, $|\text{DEC} - \text{DEC}_{\text{eRASS1}}| < 3 [h_{70}^{-1} \text{Mpc}]/D_l$, $\ln(0.1) < \ln(M_{200}/10^{14} h_{70}^{-1} M_\odot) < \ln 50$, and $\ln 1 < \ln c_{200} < \ln 30$. Regarding halo ellipticity and orientation angle, we use $-1 < e < 1$ and $0 < \phi_e < 2\pi$ to avoid an artificial boundary around $e = 0$ and $\phi_e = 0, \pi$ and then use absolute values for e and superimpose a double-peak posterior distribution for ϕ_e in the estimation. All parameters are estimated using a central biweight estimation from marginalized posterior distributions to down-weight outliers in skewed distributions.

3. Results

3.1. Cluster sample

The X-ray count-rate (CR) is estimated in the soft-band (0.2-2.3 keV) with correction of Galactic absorption (Bulbul et al. 2024). The CR of the eRASS1-HSC clusters has a weak dependence on redshift (left panel of Figure 1), as a way to trace the CR selection function. The average and median CRs are $0.91_{-0.14}^{+0.19}$ and 0.56, respectively. When we remove the first two with the highest CR, the average drops to 0.66. The richness is measured by an adapted version of the redMaPPer (Rykoff et al. 2014) algorithm (Kluge et al. 2024). The lower boundary of the cluster richness λ (the right panel of Figure 1) at high redshift ($z \gtrsim 0.6$) is higher than at low redshift ($z \lesssim 0.4$). This indicates that less massive clusters are harder to detect at higher redshifts (Clerc et al. 2024). We effectively adopt the detection threshold $\lambda = 30$ at $z < 0.45$ and 3 at $z > 0.6$ and a linear function between the two redshifts to consider the selection function in the mass-richness scaling relation.

We match the eRASS1 clusters in the HSC footprint to existing cluster catalogues (Abell 1958; Zwicky et al. 1961; Wen

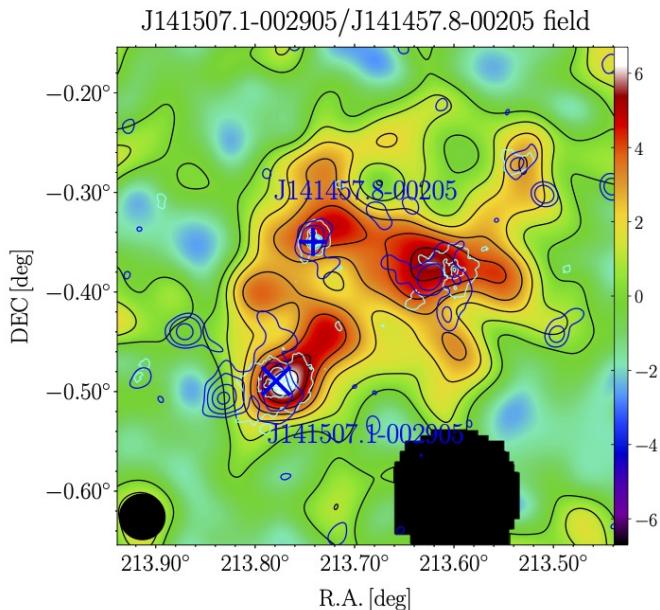


Fig. 3. Mass map for the J141507.1-002905 and J141457.8-00205 field ($30' \times 30'$). The black contours represent the reconstructed WL mass map spaced in units of 1σ bootstrapping error. The diameter of the black circle in the lower left corner represents the Gaussian smoothing FWHM=400 kpc in the mass reconstruction. Blacked-out areas are the masked regions of bright stars. The blue + and \times are positions of J141507.1-002905 and J141457.8-00205, respectively. The system is MCXC J1415.2-0030 (Piffaretti et al. 2011). The blue and cyan contours are the eRASS1 and *XMM-Newton* X-ray contours (Miyaoka et al. 2018), respectively. An X-ray bright point source in the western component is removed in the *XMM-Newton* contours. It was properly identified when the eRASS1 cluster catalogue was constructed. At the same time, diffuse X-ray emission in the *XMM-Newton* image appeared even after removing the X-ray point source thanks to higher angular resolution. The system is composed of three components with S/N $\sim 6.7\sigma$ for J141457.8-00205, $\sim 4.7\sigma$ for J141507.1-002905, and $\sim 5.3\sigma$ for the western component.

et al. 2009; Oguri et al. 2018; Koester et al. 2007; Gal et al. 2009; Goto et al. 2002; Von Der Linden et al. 2007; Dietrich et al. 2007; Popesso et al. 2004; Mehrrens et al. 2012; Hilton et al. 2021), as summarized in Table 1. The tolerance of cross-matching is 3 arcmin for the spatial separation and $|z - z_{\text{eRASS1}}| < 0.05$. If there are multiple-associations of optically selected clusters, the priority is given to putting WHL clusters (Wen et al. 2009) or HSC Camira clusters (Oguri et al. 2018). From the well-known cluster catalogues, we find 12 Abell clusters (Abell 1958), 2 Zwicky clusters (Zwicky et al. 1961), 2 X-ray clusters, or 5 SZ clusters (Hilton et al. 2021) in the sample. As one of the samples, Figure 3 shows the mass map overlaid with X-ray contours from eRASS1 and *XMM-Newton* data for J141507.1-002905 and J141457.8-00205 field, which is known as MCXC J1415.2-0030 (Piffaretti et al. 2011).

A visual inspection of the purity was carried out using the HSC images, the publicly available spectroscopic redshifts, and the spatial distribution of the red-sequence galaxies. It would be difficult to do this with each of the over 5,000 clusters of the primary sample (Ghirardini et al. 2024), but it is practically possible in the current HSC sample. The HSC images are extracted with $4' \times 4'$ centered on the centroid of the eRASS1 cluster. We overlay spectroscopic redshifts from the publicly

available catalogues (Baldry et al. 2018; Aguado et al. 2019; Lilly et al. 2009; Colless et al. 2003) and monitor the difference with the eRASS1 redshifts. We construct Gaussian smoothing maps (FWHM= $0.2 h_{70}^{-1}$ Mpc) of the number distribution of red-sequence galaxies selected in the colour-magnitude plane following Nishizawa et al. (2018); Okabe et al. (2019). The apparent z-band magnitudes of the red-sequence galaxies are brighter than the observer-frame magnitude with the constant z-band absolute magnitude of $M_z = -18$ ABmag and the limiting apparent magnitude $m_z = 25.5$. We adopted K-correction in conversion between apparent and absolute magnitudes taking into account passive evolution. Thereafter, we refer to clusters with and without optical counter-parts as association and mis-association clusters, respectively.

Based on the spectroscopic redshifts, we find three mis-association clusters; J114647.4-012428, J123108.4+003653, and J124503.8-002823 (Figure 4). Although we examine the galaxy overdensities sliced by each redshift, we cannot find any significant excess, as shown by the white contours. The X-ray centroid of J114647.4-012428 (left panel, $z = 0.33$) is associated with two ellipticals at $z \sim 0.14$. WHL J1146416-012324 with a close redshift of $z = 0.3318$ is 1.9 arcmin away from J114647.4-012428. The X-ray emission of J123108.4+003653 (middle panel, $z = 0.47$) is associated with two galaxies identified as MCXC J1231.0+0037 at $z \sim 0.023$. WHL J123122.9+003718 at $z = 0.4354$ is 3.6 arcmin away from J123108.4+003653 outside the HSC image (Figure 4). The X-ray emission from J124503.8-002823 (right panel, $z = 0.23$) is apparently from a nearby spiral galaxy, NGC 4666. WHL J124454.5-002640 at $z = 0.231$ is 3.3 arcmin away from J124503.8-002823, and its galaxy concentration is found.

We note that the fraction of the mis-association clusters in the HSC-SSP field, $3/78 \sim 4\%$, is consistent with the $\sim 95\%$ purity of the primary clusters (Clerc et al. 2024; Kluge et al. 2024).

3.2. Weak-lensing mass measurements

We first calculate the signal-to-noise ratio (S/N) of the reduced tangential shear profile by $(\sum_{ij} \Delta \Sigma_{+,i} C_{ij}^{-1} \Delta \Sigma_{+,j})^{1/2}$, where the indexes i and j denote the i -th and j -th radial bins, respectively. The average and median S/N are 4.5 and 4.3, respectively. In the CR and z plane (left panel in 1), the S/N is higher for clusters with higher CR around $z \sim 0.1 - 0.4$, because the clusters have good lensing efficiency and a large number of background galaxies. The more clear feature is found in the richness and z plane (right panel of Figure 1). The S/N tends to be higher for the clusters in the upper left corner of the figure.

The individual WL masses for the 72 association clusters are shown in Table 1. Among all the 78 clusters, we cannot measure WL masses of the three association clusters and the three mis-association clusters. The number of non-measurable clusters in the 75 association clusters is consistent with an expectation computed by mock catalogue using a realistic number density of background galaxies (see Appendix B and Figure B.1). The measurement uncertainty for 9 association clusters is too large, and thus the upper limit of WL masses is only constrained. We refer to the 12 association clusters above, whose WL masses at $\Delta = 500$ are difficult or impossible to measure, as poor-fit clusters (Table 1). The WL masses as a function of the redshift are shown in Figure 2. At higher redshifts, the WL masses tend to be larger, and at lower redshifts ($z \lesssim 0.2$) they are distributed over a wide range of masses. The modelled distribution of the

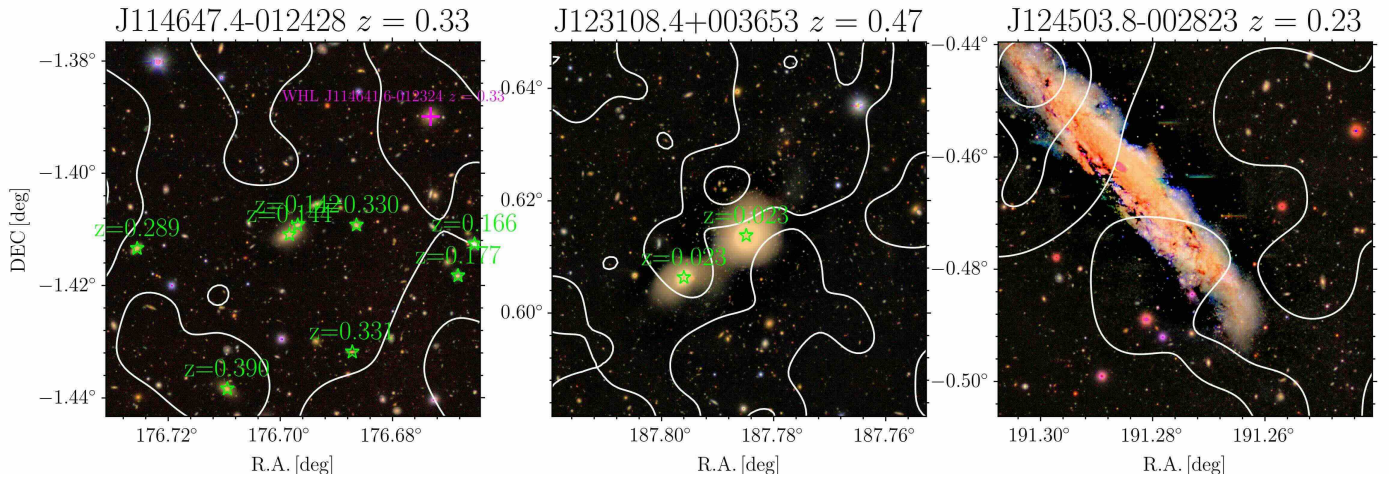


Fig. 4. The HSC images for mis-association clusters. Overlaid with white contours representing red galaxy distribution, stepped by 2 galaxies per each pixel above 2 galaxies.

WL masses in the parent population obtained by scaling relation analysis (see the details in Sec 3.4) follows this trend.

Table 1. Cluster properties and their NFW weak-lensing parameters of M_{500}^{WL} , M_{200}^{WL} , and c_{200}^{WL} . ^a is the eRASS1 cluster name. ^b is the alt-name from literature by matching within 3 arcmin from the centroid of the eRASS1 cluster, though the cluster denoted by [†] has 3.5 arcmin offset distance. ^c is the cluster redshift. ^d is cluster richness, ^e is a WL mass at $\Delta = 500$, ^f is a WL mass at $\Delta = 200$, ^g is a WL concentration parameter at $\Delta = 200$, λ . * represents the mis-association clusters by visual inspection. † : poor-fit clusters.

Name ^a	alt-name ^b	z ^c	Richness ^d , λ	$M_{500}^{\text{WL,e}}$, [$10^{14} h_{70}^{-1} M_{\odot}$]	$M_{200}^{\text{WL,f}}$, [$10^{14} h_{70}^{-1} M_{\odot}$]	$c_{200}^{\text{WL,g}}$
J083652.6+030000	WHL J083651.5+030001	0.189	41.68 ± 3.39	4.55 ^{+2.10} _{-1.45}	6.54 ^{+3.69} _{-2.72}	4.08 ^{+18.85} _{-4.08}
J084306.7+002834	WHL J084305.1+002847	0.270	30.15 ± 1.98	1.64 ^{+0.87} _{-0.70}	2.22 ^{+1.40} _{-1.03}	5.87 ^{+9.23} _{-2.99}
J084342.8+040323	WHL J084343.1+040335	0.208	20.42 ± 2.65	1.72 ^{+1.06} _{-0.90}	2.25 ^{+1.74} _{-1.74}	7.34 ^{+11.80} _{-7.34}
J084527.7+032736	ZwCl 0842.8+0336 / WHL J084528.3+032638	0.326	109.32 ± 5.40	5.24 ^{+1.62} _{-1.35}	6.99 ^{+2.78} _{-2.10}	6.22 ^{+5.38} _{-2.58}
J085029.4+001453	WHL J085023.9+001536	0.196	63.28 ± 4.34	2.82 ^{+1.28} _{-1.02}	4.81 ^{+3.45} _{-2.07}	2.08 ^{+3.19} _{-1.93}
J085217.5-010126 [†]	WHL J085216.7-010136	0.459	89.51 ± 5.09	1.20 ^{+1.53} _{-1.20}	1.61 ^{+2.27} _{-1.61}	6.20 ^{+30.66} _{-6.20}
J085230.8+002509	WHL J085230.3+002511	0.283	41.38 ± 3.06	2.87 ^{+1.11} _{-0.89}	3.72 ^{+1.73} _{-1.28}	7.62 ^{+6.44} _{-3.08}
J085435.8+003858	WHL J085436.6+003833 / HSCS J085437+003946	0.110	22.37 ± 2.57	1.95 ^{+0.91} _{-0.76}	2.74 ^{+1.51} _{-1.13}	4.62 ^{+6.65} _{-2.68}
J085751.0+031014	ABELL 0732 / WHL J085754.0+031035	0.204	89.35 ± 4.60	3.34 ^{+1.32} _{-1.06}	4.51 ^{+2.23} _{-1.60}	5.79 ^{+4.57} _{-2.45}
J085932.4+030832	WHL J085932.3+030841	0.197	45.27 ± 3.62	3.35 ^{+1.21} _{-1.00}	4.67 ^{+2.11} _{-1.59}	4.85 ^{+3.69} _{-2.03}
J090131.4+030055	WHL J090121.9+030208	0.196	60.05 ± 5.23	2.45 ^{+0.99} _{-0.91}	3.13 ^{+1.55} _{-1.19}	8.61 ^{+14.50} _{-8.61}
J091414.7+001922	WHL J091422.8+001658	0.167	19.35 ± 5.64	1.29 ^{+1.10} _{-1.11}	2.48 ^{+2.66} _{-1.75}	1.47 ^{+40.37} _{-1.47}
J091453.6+041611	NSC J091454+041559	0.143	27.60 ± 2.84	2.43 ^{+1.63} _{-1.06}	3.48 ^{+2.50} _{-2.50}	4.12 ^{+17.53} _{-4.12}
J091608.3-002355	ABELL 0776 / WHL J091605.7-002324 / HSCS J091606-002338	0.330	105.57 ± 5.16	8.78 ^{+3.04} _{-2.46}	14.15 ^{+6.63} _{-4.57}	2.54 ^{+1.37} _{-1.01}
J092050.7+024512	WHL J092049.7+024514 / HSCS J092050+024606	0.279	65.36 ± 10.62	2.54 ^{+1.40} _{-1.08}	4.06 ^{+3.48} _{-2.15}	2.62 ^{+11.72} _{-2.62}
J092121.0+031735	WHL J092121.1+031713	0.347	106.39 ± 3.94	5.86 ^{+1.56} _{-1.32}	7.68 ^{+2.40} _{-1.95}	7.21 ^{+3.26} _{-2.04}
J092210.0+034626	WHL J092207.6+034558	0.279	91.24 ± 4.55	3.73 ^{+1.54} _{-1.31}	6.64 ^{+3.61} _{-2.51}	1.82 ^{+1.65} _{-1.07}
J093025.3+021707	WHL J093024.2+021728	0.540	75.50 ± 4.36	4.62 ^{+3.82} _{-2.54}	6.24 ^{+7.01} _{-4.97}	5.85 ^{+32.71} _{-5.85}
J093150.9-002220	WHL J093151.0-002213	0.346	23.91 ± 4.05	2.73 ^{+1.56} _{-1.15}	3.85 ^{+2.87} _{-1.78}	4.51 ^{+5.85} _{-2.56}
J093459.9+005438	WHL J093500.7+005414	0.377	47.25 ± 3.00	3.02 ^{+2.17} _{-1.83}	4.90 ^{+3.98} _{-2.75}	2.49 ^{+43.08} _{-2.49}
J093512.7+004735	WHL J093513.0+004846	0.365	128.92 ± 5.33	13.78 ^{+12.88} _{-6.82}	29.15 ^{+43.73} _{-29.15}	1.17 ^{+1.65} _{-1.17}
J093521.3+023222	WHL J093522.5+023324	0.499	136.83 ± 5.88	5.03 ^{+2.80} _{-2.34}	6.36 ^{+4.32} _{-3.37}	9.45 ^{+108.49} _{-9.45}
J094023.3+022824	ABELL 0847 / WHL J094024.6+022840	0.154	53.12 ± 3.11	6.77 ^{+1.67} _{-1.43}	11.43 ^{+3.83} _{-2.86}	2.15 ^{+0.92} _{-0.72}
J094611.9+022201	ABELL 0869 / WHL J094612.0+022208	0.123	20.81 ± 1.60	1.94 ^{+0.93} _{-0.74}	2.95 ^{+1.86} _{-1.27}	3.20 ^{+4.57} _{-1.92}
J094844.3+020019		0.490	20.93 ± 6.53	4.64 ^{+2.95} _{-2.14}	7.03 ^{+5.45} _{-5.45}	3.24 ^{+28.70} _{-3.24}
J095341.6+014200	SDSS-C4-DR3 1212 / RXC J0953.6+0142	0.109	10.82 ± 1.78	1.96 ^{+0.95} _{-0.77}	2.67 ^{+1.66} _{-1.18}	5.59 ^{+7.56} _{-3.12}
J095736.6+023430	WHL J095737.0+023426	0.382	41.68 ± 3.71	2.32 ^{+1.37} _{-1.17}	3.77 ^{+2.64} _{-1.88}	2.48 ^{+3.96} _{-1.77}
J095858.4-001323 [†]	SDSS CE J149.746765-00.198446	0.175	48.87 ± 3.17	0.55 ^{+0.64} _{-0.55}	0.72 ^{+1.01} _{-0.72}	7.43 ^{+21.34} _{-7.43}
J101851.0-010105 [†]	WHL J101852.4-005857	0.114	9.20 ± 1.32	0.26 ^{+0.38} _{-0.26}	0.37 ^{+0.60} _{-0.37}	4.13 ^{+9.01} _{-4.13}
J102250.3-000309	SDSS CE J155.708923-00.050793	0.302	29.02 ± 2.08	1.56 ^{+1.20} _{-1.02}	2.05 ^{+2.17} _{-1.60}	7.06 ^{+33.71} _{-7.06}
J105039.5+001707	SDSS J1050+0017 Cluster	0.597	64.21 ± 3.44	9.38 ^{+4.92} _{-4.22}	11.83 ^{+7.89} _{-7.89}	9.47 ^{+13.43} _{-9.47}
J111111.5+004454	ABELL 1191 / WHL J111111.2+004508	0.188	44.23 ± 4.49	2.34 ^{+0.93} _{-0.76}	3.14 ^{+1.51} _{-1.14}	6.00 ^{+5.84} _{-2.70}
J112626.5+003625 [†]		0.305	10.84 ± 1.55	0.45 ^{+0.65} _{-0.45}	0.70 ^{+1.08} _{-0.70}	2.86 ^{+4.90} _{-2.86}
J112818.3-005859	SDSS CE J172.069611-00.983567	0.456	74.51 ± 3.60	10.40 ^{+4.07} _{-3.22}	17.56 ^{+9.81} _{-6.31}	2.15 ^{+1.28} _{-0.93}
J113655.7+000612	WHL J113658.7+000602	0.585	124.71 ± 10.25	5.07 ^{+4.01} _{-3.52}	9.32 ^{+13.31} _{-7.59}	1.66 ^{+3.07} _{-1.66}
J113843.1+031510 [†]	BLOX J1138.7+0315.6	0.137	8.29 ± 1.34	-	-	-
J114441.9+004414	SDSS CE J176.174454+00.738345 / HSCS J114441+004304	0.334	19.87 ± 1.96	2.31 ^{+1.47} _{-1.20}	3.02 ^{+2.79} _{-1.48}	7.11 ^{+26.43} _{-7.11}
J114647.4-012428*	WHL J114641.6-012324	0.331	5.31 ± 1.23	-	-	-

Table 1. continued.

Name ^a	alt-name ^b	z ^c	Richness ^d , λ	M_{500}^{WLe}	M_{200}^{WLI}	c_{200}^{WLG}
J115019.2-003637	ABELL 1392 [†] / WHL J115018.7-003631 / HSCS J115028-003723	0.142	32.67 ± 2.68	3.19 ^{+1.03} _{-0.83}	4.21 ^{+1.65} _{-1.23}	6.73 ^{+3.92} _{-2.31}
J115208.5-004726 [‡]	WHL J115205.2-004616 / HSCS J115212-004511	0.259	4.84 ± 1.34	0.02 ^{+0.31} _{-0.02}	0.03 ^{+0.44} _{-0.03}	14.18 ^{+266.93} _{-14.18}
J115214.5+003057	WHL J115214.2+003126 / HSCS J115216+003055	0.470	85.97 ± 3.88	9.12 ^{+3.16} _{-2.60}	13.13 ^{+5.65} _{-4.22}	4.08 ^{+1.89} _{-1.33}
J115235.7+035642 [‡]	WHL J115237.0+035434 / ACT-CL J1152.5+0356	0.681	67.55 ± 7.79	1.43 ^{+2.08} _{-1.43}	1.74 ^{+2.91} _{-1.74}	14.07 ^{+43.30} _{-14.07}
J115417.0+022123	ACT-CL J1154.2+0221	0.743	42.78 ± 3.56	6.06 ^{+6.01} _{-4.84}	7.97 ^{+9.62} _{-5.35}	6.96 ^{+18.28} _{-3.76}
J115620.0-001220	ABELL 1419 / WHL J115620.1-001220 / HSCS J115612-001237	0.110	22.66 ± 2.45	1.59 ^{+1.18} _{-0.95}	2.40 ^{+2.71} _{-2.40}	3.28 ^{+6.19} _{-3.28}
J120024.4+032112	ABELL 1437 / WHL J120025.3+032049	0.136	101.18 ± 4.36	7.58 ^{+1.81} _{-1.56}	12.57 ^{+4.03} _{-3.07}	2.29 ^{+0.93} _{-0.73}
J120143.7-001110	ABELL 1445 / WHL J120143.7-001104 / HSCS J120141-000953	0.170	40.73 ± 2.91	3.10 ^{+1.36} _{-1.06}	4.77 ^{+2.62} _{-1.88}	3.03 ^{+1.64} _{-1.36}
J120417.3+025402		0.149	7.91 ± 1.81	1.61 ^{+0.93} _{-0.90}	2.21 ^{+1.36} _{-1.31}	5.20 ^{+13.98} _{-5.20}
J120954.5-003328	SDSS CE J182.479843-00.560958 / HSCS J120946-003512	0.184	26.87 ± 2.24	1.78 ^{+0.96} _{-0.73}	2.27 ^{+1.51} _{-1.03}	8.93 ^{+19.24} _{-7.60}
J121016.3+022338	WHL J121017.7+022343	0.381	54.40 ± 3.42	4.94 ^{+2.34} _{-1.86}	6.43 ^{+3.82} _{-2.70}	7.39 ^{+10.53} _{-4.01}
J121336.5+025331	WHL J121334.5+025355	0.394	87.86 ± 15.88	2.57 ^{+1.86} _{-1.47}	3.48 ^{+2.51} _{-1.75}	5.80 ^{+33.75} _{-5.80}
J122420.6+021206	WHL J122422.0+021211	0.451	46.70 ± 3.38	6.48 ^{+1.14} _{-2.08}	10.18 ^{+3.17} _{-3.71}	2.79 ^{+1.64} _{-1.16}
J122528.9+004237 [‡]	WHL J122529.3+004334 / XMMXCS J122528.0+004229.2	0.242	17.91 ± 4.67	-	-	-
J122644.5-003724	NSC J122644-003738	0.159	36.01 ± 2.30	0.80 ^{+0.69} _{-0.58}	1.18 ^{+1.01} _{-0.77}	3.50 ^{+18.06} _{-3.50}
J123108.4+003653 [*]		0.473	9.60 ± 9.27	-	-	-
J123755.2-001611	ABELL 1577	0.141	37.91 ± 2.41	1.41 ^{+0.72} _{-0.56}	1.88 ^{+1.27} _{-1.04}	6.48 ^{+18.95} _{-6.48}
J124503.8-002823 [*]		0.231	34.71 ± 20.69	-	-	-
J125035.8+003646	ACT-CL J1250.6+0036	0.634	38.93 ± 3.29	3.77 ^{+3.71} _{-3.71}	4.95 ^{+5.61} _{-4.95}	6.65 ^{+8.63} _{-6.65}
J131129.4-012026	ABELL 1689 / WHL J131132.1-011946	0.184	183.14 ± 5.32	16.50 ^{+2.55} _{-2.28}	21.08 ^{+4.52} _{-3.72}	8.58 ^{+7.24} _{-3.30}
J134840.1+003907 [‡]	SDSS CE J207.185104+00.662313	0.422	33.69 ± 2.49	0.87 ^{+1.14} _{-0.87}	1.70 ^{+2.02} _{-1.67}	1.41 ^{+14.08} _{-1.41}
J135326.5+000255	WHL J135326.3+000248	0.107	13.57 ± 1.95	1.64 ^{+0.79} _{-0.64}	2.33 ^{+1.36} _{-1.01}	4.39 ^{+4.98} _{-2.29}
J135424.2-010250	ZwCl 1351.8-0048 / WHL J135421.8-010000	0.152	52.01 ± 3.51	4.08 ^{+1.64} _{-1.28}	6.45 ^{+3.78} _{-2.38}	2.74 ^{+2.09} _{-1.35}
J140707.1-001450	SDSS CE J211.765610-00.254689 / HSCS J140709-001436	0.554	74.25 ± 3.73	2.88 ^{+2.63} _{-2.24}	4.51 ^{+5.49} _{-3.12}	2.83 ^{+10.42} _{-2.83}
J141452.4+001316 [‡]	SDSS CE J213.734085+00.213623	0.121	24.87 ± 2.31	0.27 ^{+0.52} _{-0.27}	0.49 ^{+1.12} _{-0.49}	1.80 ^{+4.48} _{-1.80}
J141457.8-002050 [‡]	SDSS-C4 1031	0.133	99.48 ± 4.26	0.61 ^{+1.78} _{-0.61}	0.84 ^{+2.95} _{-0.84}	4.44 ^{+16.28} _{-4.44}
J141507.1-002905	ABELL 1882 / WHL J141508.4-002935	0.133	70.83 ± 4.07	2.34 ^{+4.10} _{-1.19}	3.01 ^{+6.84} _{-2.66}	8.19 ^{+16.50} _{-7.59}
J141547.1+001530	WHL J141548.8+001537 / HSCS J141547+001709	0.128	29.03 ± 3.25	1.56 ^{+0.84} _{-0.63}	2.28 ^{+1.61} _{-1.03}	3.85 ^{+5.55} _{-2.16}
J142016.3+005716	WHL J142016.6+005719	0.499	60.52 ± 2.59	6.64 ^{+2.32} _{-1.94}	10.10 ^{+4.46} _{-3.31}	3.19 ^{+1.97} _{-1.31}
J142724.6-001509	SDSS CE J216.852905-00.249845 / HSCS J142723-001638	0.164	25.85 ± 7.55	1.47 ^{+0.86} _{-0.65}	2.17 ^{+1.69} _{-1.07}	3.58 ^{+5.31} _{-2.28}
J143044.6+004815	WHL J143042.1+004902	0.311	36.78 ± 2.61	7.77 ^{+3.53} _{-2.40}	14.82 ^{+13.79} _{-5.75}	1.50 ^{+1.11} _{-0.90}
J143121.5-005336	SDSS CE J217.834290-00.898368	0.402	70.96 ± 3.67	2.73 ^{+1.40} _{-1.09}	3.49 ^{+2.24} _{-1.53}	8.40 ^{+14.27} _{-4.72}
J143736.1-001740	ABELL 1938 / WHL J143743.2-001512 / HSCS J143741-001819	0.140	44.59 ± 3.10	1.70 ^{+1.02} _{-0.89}	3.59 ^{+2.13} _{-1.58}	1.14 ^{+1.13} _{-0.73}
J144050.2+004103 [‡]	WHL J144048.9+004020	0.545	30.01 ± 4.06	-	-	-
J144133.6-005418	SDSS CE J220.382751-00.899307 / ACT-CL J1441.5-0053	0.543	51.99 ± 3.73	5.82 ^{+3.25} _{-2.63}	12.66 ^{+10.81} _{-5.91}	1.06 ^{+1.14} _{-0.79}
J144309.6+010214	WHL J144309.3+010211	0.534	60.35 ± 3.95	6.02 ^{+4.18} _{-2.71}	8.38 ^{+8.15} _{-4.27}	4.83 ^{+9.34} _{-4.17}
J144950.6+005558	WHL J144945.7+005705 / HSCS J144954+005717	0.409	47.60 ± 3.44	3.67 ^{+2.55} _{-1.83}	6.70 ^{+8.59} _{-3.59}	1.69 ^{+2.56} _{-1.69}
J145004.7+004931	SDSS CE J222.476242+00.844170 / ACT-CL J1450.0+0049	0.382	61.27 ± 5.61	3.45 ^{+2.45} _{-1.59}	4.62 ^{+4.32} _{-2.37}	6.12 ^{+10.83} _{-4.91}
J145218.8+001002	WHL J145218.9+001027 / HSCS J145218+000942	0.586	90.04 ± 5.31	6.42 ^{+8.32} _{-6.04}	13.29 ^{+17.24} _{-13.29}	1.20 ^{+6.43} _{-1.20}
J145459.3-011455	SDSS CE J223.754150-01.250201	0.314	26.06 ± 2.48	2.64 ^{+1.25} _{-1.03}	4.05 ^{+2.40} _{-1.74}	3.08 ^{+4.43} _{-1.80}

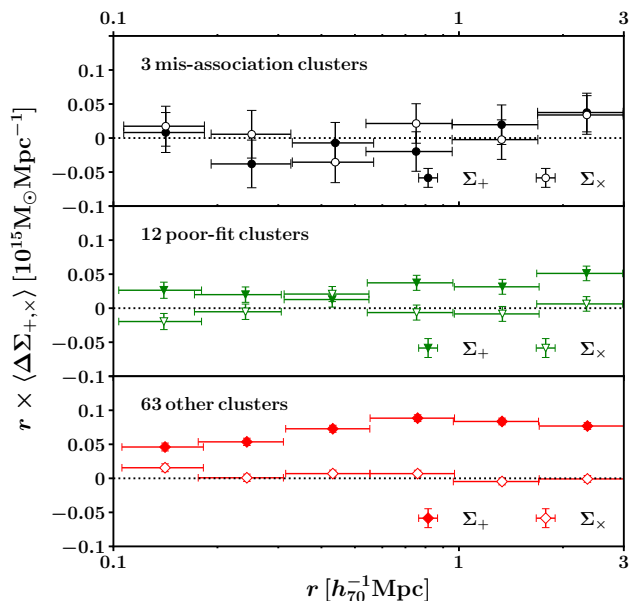


Fig. 5. Stacked profiles for the 3 mis-association clusters (top), the 12 poor-fit clusters (middle), and the 63 other clusters (bottom). The y-axis represents $r \times \langle \Delta \Sigma_{+,x} \rangle$ (filled colours) or $r \times \langle \Sigma_{x} \rangle$ (open colours). The + components for the 63 other clusters and the 12 poor-fit clusters are higher than the \times components, while both the + and \times components for 3 mis-association clusters are consistent with the null.

3.3. Stacked tangential shear profiles

We computed the stacked tangential shear profiles for the 3 mis-association clusters, the 12 poor-fit clusters, and 63 other association clusters (Figure 5). The number of bins is six because of the small number of background galaxies for the 3 mis-association clusters. To visualize the null signal for the mis-association clusters, we use r times the tangential shear, $\langle \Sigma_{+} \rangle$, or the 45-degree rotated component, $\langle \Sigma_{x} \rangle$, for the y axis. The tangential shear component for the mis-association clusters is comparable to the 45-degree rotated component and consistent with the null, supporting the visual inspection result (Sec. 3.1). In contrast, the lensing signals for the poor-fit and remaining 63 clusters are significantly detected with $S/N = 7.0$ and 34.0 , respectively.

We divide the remaining 63 clusters into three samples by redshift; $0.4 < z$, $0.2 < z \leq 0.4$, and $0.1 < z \leq 0.2$ (Figure 6). The S/N s are 12.9, 19.1, and 23.6 in the order of higher redshift, respectively. The curvature in the tangential shear profile is clearly found. The tangential shear profile for the poor-fit clusters shows a depletion in an intermediate radius of $0.2 \lesssim r \lesssim 1 h_{70}^{-1} \text{Mpc}$ (Sec 3.8).

3.4. Mass-richness-CR relation

We computed scaling relations between the extinction corrected CR and the WL masses and between the richness of the cluster and the WL masses of the 72 individual clusters, excluding 3 clusters with no mass measurements (Figure 7). The CR is multiplied by the square of the luminosity distance, $D_L(z)$, and the inverse square of $E(z) = \sqrt{\Omega_{m,0}(1+z)^3 + \Omega_{\Lambda,0}}$ to correct the redshift evolution (Chiu et al. 2022; Ghirardini et al. 2024), spec-

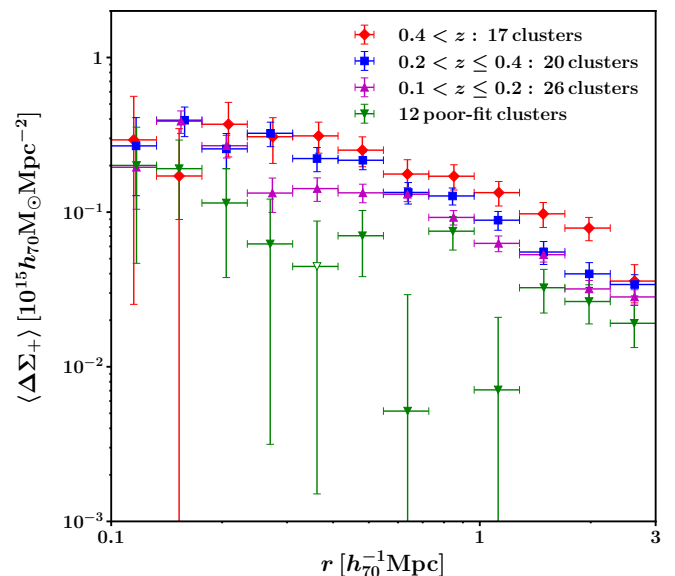


Fig. 6. Stacked tangential profiles for 3 subsamples divided by redshift ranges of $0.4 < z$ (red diamonds), $0.2 < z \leq 0.4$ (blue squares), and $0.1 < z \leq 0.2$ (magenta upward triangles), and the 12 poor-fit clusters (green downward triangles). The filled and open symbols denote positive and negative values, respectively.

ified as

$$CR \left(\frac{D_L(z)}{D_L(z_p)} \right)^2 \left(\frac{E(z)}{E(z_p)} \right)^{-2} \quad (16)$$

where z_p is a pivot redshift 0.21 as a lensing weight average from stacked lensing analysis. For the logarithmic quantity, we express the correction term as

$$E_x(z) = -2 \ln(D_L(z)/D_L(z_p)) + 2 \ln(E(z)/E(z_p)).$$

Both the corrected CR and the richness are highly correlated with the WL masses (Figure 7). To quantify the relationships between mass, CR, and richness, we adopt the trivariate scaling relations, including the relation between the WL masses (M_{500}^{WL}) and the true masses (M_{500}^{true}), the so-called WL mass calibration. In general, the WL mass calibration consists of two effects: astrophysical (intrinsic) properties and observational conditions. The former is mainly due to the orientation of elliptical halos, the presence of subhalos, and their surroundings. The adaptive choice of radial bins could reduce these effects as much as possible (Okabe et al. 2016). The latter is associated with the number of background galaxies. When the gravitational lensing signal is synthesized with the intrinsic ellipticity of a small number of background galaxies, the observed S/N is randomly determined and the masses that can be measured are limited to those with a selectively high bias. Since the number density of our background galaxies strongly depends on cluster redshifts (Figures 2 and B.1), we cannot rule out such a selection bias in successful individual WL mass measurements. To quantify selection bias, we performed mock simulations empirically representing observational conditions using a spherical NFW model (see details in Sec. B). We made 3000 mock shape catalogues and repeated our analysis without lensing effect from large-scale structure. The measurable fraction decreases as the cluster redshift increases

and the mass decreases, so the measured WL mass has a higher positive bias as the cluster redshift increases and the mass decreases. With a selection function, the WL mass calibration is well described by a redshift-dependent linear equation of the logarithmic quantities (eq. 17) and is used as prior in a regression analysis. We note that our WL mass calibration based on two parameters is different from the one-parameter case (Chiu et al. 2022; Grandis et al. 2024).

We use the hierarchical Bayesian regression method (Akino et al. 2022) to infer the true mass distribution of the parent population, taking into account the selection effect. We assume that the logarithm of the true mass follows a Gaussian distribution $\mathcal{N}(\mu(z), \sigma(z))$ of which mean (μ) and standard error (σ) are a polynomial function of $F(z) = \ln((1+z)/(1+z_p))$. We use the 2nd order and 1st order polynomial functions for the mean and standard error, respectively. As shown in Akino et al. (2022), the model realizes well the input of multivariate scaling relations in samples of $\sim O(100)$ clusters, regardless of the shape of the parent population, such as the Gaussian distribution and the cluster mass function. Its advantage is that it is independent of the cluster mass function or cosmological parameters. We adopt the lower-limits for the corrected CR and the richness as 0.01 and the line in Figure 1, respectively. In the regression analysis, we use the following equations (see also Ghirardini et al. 2024; Grandis et al. 2024)

$$\ln\left(\frac{M_{500}^{\text{WL}}}{M_p}\right) = \alpha_{\text{WL}} + (\beta_{\text{WL}} + \delta_{\text{WL}}F(z)) \ln\left(\frac{M_{500}^{\text{true}}}{M_p}\right) + \gamma_{\text{WL}}F(z) \quad (17)$$

$$\ln\left(\frac{\text{CR}}{\text{CR}_p}\right) - E_x(z) = \alpha_{\text{CR}} + (\beta_{\text{CR}} + \delta_{\text{CR}}F(z)) \ln\left(\frac{M_{500}^{\text{true}}}{M_p}\right) + \gamma_{\text{CR}}F(z) \quad (18)$$

$$\ln\left(\frac{\lambda}{\lambda_p}\right) = \alpha_{\lambda} + (\beta_{\lambda} + \delta_{\lambda}F(z)) \ln\left(\frac{M_{500}^{\text{true}}}{M_p}\right) + \gamma_{\lambda}F(z) \quad (19)$$

where M_p , CR_p , and λ_p are a pivot mass $10^{14}h_{70}^{-1}M_{\odot}$, a pivot count-rate 1 cnt s^{-1} and a pivot richness 40, respectively. The normalization, the mass-dependent slope, the redshift-dependent slope in the normalization, and the redshift-dependent slope in the mass-related slope are expressed by α , β , γ and δ , respectively. Although the self-similar slope should be $\gamma = \delta = 0$, they quantify the deviation from the self-similar model (e.g. Bulbul et al. 2019; Chiu et al. 2022; Ghirardini et al. 2024). The intrinsic covariance (Okabe et al. 2010) is described by

$$C_{\text{int}} = \begin{pmatrix} \sigma_{\text{WL}}^2 & r_{\text{CR,WL}}\sigma_{\text{CR}}\sigma_{\text{WL}} & r_{\lambda,\text{WL}}\sigma_{\lambda}\sigma_{\text{WL}} \\ r_{\text{CR,WL}}\sigma_{\text{CR}}\sigma_{\text{WL}} & \sigma_{\text{CR}}^2 & r_{\text{CR},\lambda}\sigma_{\text{CR}}\sigma_{\lambda} \\ r_{\lambda,\text{WL}}\sigma_{\lambda}\sigma_{\text{WL}} & r_{\text{CR},\lambda}\sigma_{\text{CR}}\sigma_{\lambda} & \sigma_{\lambda}^2 \end{pmatrix}, \quad (20)$$

where σ and r are the intrinsic scatter of the left-hand-side quantities of eqs. (17)–(19) and the intrinsic coefficient between two variables, respectively. We assume that the intrinsic covariance is independent of the redshift. We use the WL mass bias parameters as priors (Appendix. B), taking into account their error covariance matrix.

We first performed a regression analysis for three cases: (1) $r_{\text{CR,WL}} = r_{\lambda,\text{WL}} = 0$, (2) $\delta = 0$, and (3) all the free parameters. The resulting parameters are shown in Table 2. The intrinsic coefficients, $r_{\text{CR,WL}}$ and $r_{\lambda,\text{WL}}$, are not well constrained in the three cases and are consistent with 0. In contrast to Ghirardini et al. (2024), the errors of redshift-dependent slopes δ and γ are large

because of our small sample size. We then fix $r_{\text{CR,WL}} = r_{\lambda,\text{WL}} = 0$ and $\delta = 0$, which is referred to as (4).

We compare the models using Akaike’s information criterion (AIC) and Bayesian information criterion (BIC) to evaluate which model is considered closer to the truth. The deviations of the AIC and BIC of (1)–(3) from (4) give larger values with $+5 \sim +22$. When we additionally fix $\gamma = 0$, ΔAIC and ΔBIC becomes even worse by $+9$ and $+3$, respectively. Therefore, we focus on the result of (4), as shown in Fig. 7. The blue solid and magenta solid lines are the best-fit scaling relations with the WL and true masses (Fig. 7), respectively.

The mass-dependent slope for CR and mass scaling relation is consistent with 1. The mass-dependent slope for the richness and mass scaling relation supports the fact that the number of cluster members is proportional to the cluster mass. Although the redshift dependencies of the normalizations are not well constrained, the normalization for the CR and the richness are likely to increase and decrease as the redshift increases, respectively. The intrinsic scatter for the two scaling relations is $\sim 30\%$. We find that the intrinsic coefficient between the CR and richness is consistent with zero.

Stacked lensing results are indicated by blue diamonds, regardless of the success of individual mass measurements. The three sub-samples are divided by the richness with $\lambda \leq 40$, $40 < \lambda < 70$, and $70 \leq \lambda$. Since the number of background galaxies and the lensing efficiency for individual clusters are different from each other, we compute the average values with a lensing weight of $w_{\text{lens},i} = \sum_i \Sigma_{\text{cr}}^{-1}(z_{l,j}, z_{s,i}) / \sum_{i,j} \Sigma_{\text{cr}}^{-1}(z_{l,j}, z_{s,i})$, where i and j are the indexes for the clusters and their background galaxies, respectively. The stacked quantities coincide with the baseline with the WL mass.

The Bayesian analysis also gives us the parent population of the true mass M_{500}^{true} , which leads to the M_{500}^{WL} distribution of the parent population. As shown in Figure 2, the M_{500}^{WL} distribution represents well the measured M_{500}^{WL} of the observed sample. When we change the order polynomial function to 1 or 3, the result does not change and use the 2nd order polynomial function for the standard error, both the AIC and BIC get worse by $+1$ and $+4$, respectively. The current model is thus sufficient to describe the sample.

We artificially change the intrinsic scatter of the WL mass calibration to $\sigma_{\text{WL}} = 0.214$ calibrated with synthetic weak-lensing observations (Umetsu et al. 2020) of 639 cluster halos in a dark-matter-only realization of BAHAMAS simulations (McCarthy et al. 2017) at a single redshift $z = 0.25$. The same analysis was carried out with only the normalization in the WL mass calibration parameters set to this value. We find that γ and σ_{int} for the two scaling relations change by $\sim +20\%$ and $\sim -10\%$, respectively.

Since our WL mass measurements do not use any informative priors, it is easy to find out the outliers, such as the poor-fit clusters. When we remove the 12 poor-fit clusters, we find that the baseline parameters do not change significantly and the intrinsic scatter of the CR and the richness become $\sim 8\%$ lower, although they are consistent with each other within 1σ .

3.5. Mass-Concentration Relation

Numerical simulations (e.g. Bullock et al. 2001; Bhattacharya et al. 2013; Child et al. 2018; Diemer & Joyce 2019; Ishiyama et al. 2021) predict that the halo concentration for the NFW mass model increases with decreasing halo mass and redshift. Such an anti-correlation between mass and concentration can be

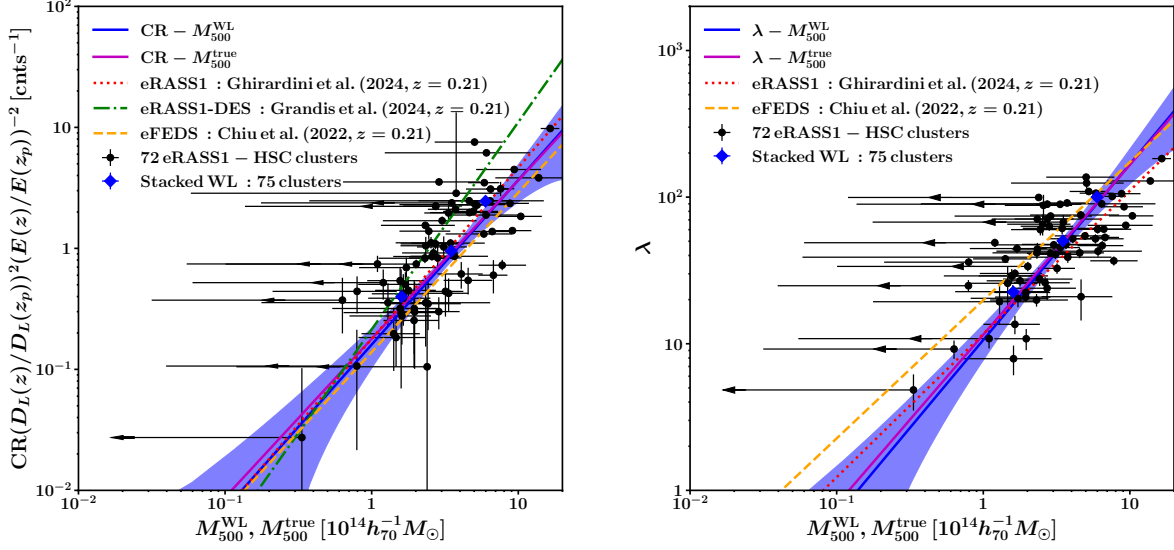


Fig. 7. Scaling relations between the count-rate (*left*) the richness (*right*) and the WL (M_{500}^{WL}) and true masses (M_{500}). The black circles and blue diamonds denote the individual WL masses of the 72 association clusters and the stacked WL masses for the three sub-samples divided by richness from the 75 association clusters, respectively. The upper bounds of the WL masses and the associated arrows are used for the poor-fit clusters. The blue and magenta solid lines are the best-fit scaling relation with respect to the WL masses and the true masses ($\delta_{\text{CR}} = \delta_{\lambda} = r_{\text{CR,WL}} = r_{\lambda,\text{WL}} = 0$), respectively. The blue region is the 1σ uncertainty of the scaling relation with the WL masses. The blue dotted, green dotted, orange dashed lines are the results of eRASS1 (Ghirardini et al. 2024), eRASS-DES (Grandis et al. 2024) and eFEDS (Chiu et al. 2022), respectively.

Table 2. Best-fit parameters for the mass-richness-CR relation.

	(4)	(1)	(2)	(3)
α_{CR}	$-1.722^{+0.318}_{-0.372}$	$-1.812^{+0.357}_{-0.426}$	$-1.400^{+0.241}_{-0.345}$	$-1.785^{+0.341}_{-0.437}$
β_{CR}	$1.310^{+0.294}_{-0.277}$	$1.388^{+0.354}_{-0.302}$	$0.995^{+0.278}_{-0.212}$	$1.361^{+0.304}_{-0.301}$
γ_{CR}	$1.984^{+1.136}_{-1.148}$	$2.570^{+2.638}_{-3.554}$	$3.374^{+1.036}_{-1.116}$	$0.139^{+1.145}_{-0.995}$
δ_{CR}	0 (fixed)	$-0.268^{+2.721}_{-2.043}$	0 (fixed)	$1.196^{+1.095}_{-0.894}$
α_{λ}	$-1.165^{+0.252}_{-0.244}$	$-1.283^{+0.381}_{-0.300}$	$-1.220^{+0.312}_{-0.237}$	$-1.176^{+0.224}_{-0.270}$
β_{λ}	$1.066^{+0.183}_{-0.216}$	$1.181^{+0.220}_{-0.265}$	$1.107^{+0.163}_{-0.210}$	$1.113^{+0.193}_{-0.190}$
γ_{λ}	$-0.368^{+0.905}_{-1.012}$	$-2.075^{+4.637}_{-3.150}$	$0.074^{+0.942}_{-1.003}$	$-0.068^{+1.252}_{-1.185}$
δ_{λ}	0 (fixed)	$0.789^{+2.402}_{-2.534}$	0 (fixed)	$-0.610^{+1.498}_{-0.884}$
σ_{CR}	$0.353^{+0.094}_{-0.135}$	$0.380^{+0.109}_{-0.147}$	$0.443^{+0.076}_{-0.090}$	$0.320^{+0.109}_{-0.184}$
σ_{λ}	$0.399^{+0.096}_{-0.128}$	$0.434^{+0.155}_{-0.151}$	$0.240^{+0.120}_{-0.162}$	$0.401^{+0.096}_{-0.101}$
$r_{\text{CR,WL}}$	0 (fixed)	0 (fixed)	$0.129^{+0.439}_{-0.587}$	$0.193^{+0.465}_{-0.639}$
$r_{\lambda,\text{WL}}$	0 (fixed)	0 (fixed)	$-0.476^{+0.681}_{-0.278}$	$0.038^{+0.517}_{-0.576}$
$r_{\text{CR},\lambda}$	$-0.036^{+0.398}_{-0.501}$	$0.085^{+0.404}_{-0.546}$	$-0.232^{+0.409}_{-0.410}$	$-0.140^{+0.400}_{-0.423}$
ΔAIC	0	+4.9	+6.1	+10.2
ΔBIC	0	+10.9	+12.0	+22.0

explained by hierarchical structure formation. The progenitors of less massive halos form first, and their characteristic central mass density is reflected by a critical density at higher redshifts. More massive halos form later, with lower mass densities than the less massive halos, and grow by mass accretion and mergers of smaller objects. Some simulations show that the concentration turns upward for the most massive halos (e.g. Prada et al. 2012; Klypin et al. 2016). This upturn feature is still controversial (e.g. Prada et al. 2012; Diemer & Kravtsov 2015; Klypin et al. 2016; Child et al. 2018). The concentration also depends on the dynamical state, that is, relaxed halos have a higher concentration than unrelaxed halos (e.g. Dutton & Macciò 2014; Klypin et al. 2016; Ishiyama et al. 2021).

The mass and concentration give us a unique opportunity to test how structures form at cluster scales. Thanks to X-ray

emissivity, X-ray centroid determination does not suffer from projection effects like optically selected clusters (e.g. Okabe & Smith 2016; Umetsu et al. 2016; Okabe et al. 2019; Umetsu et al. 2020).

The mass and concentration of the 72 association clusters for which WL masses were successfully measured are shown in Figure 8. Since these errors are correlated, the 1σ banana-shaped regions are shown in shaded gray colour. To model the mass and concentration relation, we adopt the following relation

$$\ln\left(\frac{c_{200}}{c_p}\right) = \ln c_0 + \gamma \ln\left(\frac{1+z}{1+z_p}\right) + \left(\beta + \delta \ln\left(\frac{1+z}{1+z_p}\right)\right) \ln\left(\frac{M_{200}}{10^{14} h^{-1} M_{\odot}}\right), \quad (21)$$

Table 3. Best-fit parameters for the mass and concentration relation.

	WL cal	no WL cal
$\ln c_0$	$0.019^{+0.285}_{-0.343}$	$0.160^{+0.281}_{-0.336}$
α	$-0.065^{+0.234}_{-0.202}$	$-0.101^{+0.233}_{-0.192}$
γ	$-0.500^{+1.107}_{-1.224}$	$0.436^{+0.855}_{-0.974}$
$\sigma_{\ln c}$	< 0.198	< 0.198

with $c_p = 4$ and the intrinsic scatter of σ_c . The reference redshift is set to be the lensing weight average $z_p = 0.21$ for the 72 association clusters. We take into account the correlation between the errors of mass and concentration and the WL mass calibration in the fitting (Appendix. A). Since the mass and concentration parameters are measured simultaneously, we evaluate the WL mass calibration as a mass and concentration plane with intrinsic covariance (Appendix B) and use it as a prior. Table 3 lists the best-fit parameters with and without the WL calibration, where we fix $\delta = 0$ because we cannot constrain it. In Figure 8, the best-fit and its 1σ uncertainty for the WL mass and concentration relation are shown as the blue solid line and the shaded region. The normalization of the WL mass and concentration relation is overestimated by $\sim 12\%$ compared to the true one (the magenta line). The mass-dependant slope is in good agreement with the predictions of recent numerical simulations (Bhattacharya et al. 2013; Child et al. 2018; Diemer & Joyce 2019; Ishiyama et al. 2021), though the uncertainties are too large to distinguish between negative and positive values. Figure 9 shows the redshift evolution of the normalization of the true mass and concentration relation. The error is too large to make a strong conclusion, but the normalization decreases as the redshift increases, which is consistent with the numerical simulation (Bhattacharya et al. 2013). In contrast, when we do not apply the WL mass calibration, the normalization increases as the redshift increases (blue dotted lines in Figure 9). When we remove the poor-fit clusters, we find that our results are not changed; $\ln c_0 = -0.023^{+0.305}_{-0.388}$, $\beta = -0.043^{+0.272}_{-0.215}$, and $\gamma = -0.625^{+1.102}_{-1.244}$.

We divide the clusters into two subsamples using the number of peaks in the galaxy map. To select clusters with massive galaxy subhalos, we adopt that a peak height ratio between the highest subhalo peak and the main peak is higher than 0.5. We refer to these as multiple-peak clusters and the remaining clusters as single-peak clusters. In the analysis, we use the 75 association clusters including clusters of which WL masses have not been successfully measured in order to their average properties. The halo concentration for the multiple-peak clusters is $2.40^{+0.38}_{-0.35}$, which is about 0.63 times that of the single-peak clusters $3.80^{+0.41}_{-0.38}$. The halo concentration for the single-peak clusters is in good agreement with the numerical simulations, while that for the multiple-peak clusters is $\sim 3.5\sigma$ lower than those for the given mass. The two clusters (J141507.1-002905 and J141457.8-002050) in multiple-peak clusters are members of a three-cluster system. When we exclude the two clusters, the resulting $c_{200}^{\text{WL}} = 2.52^{+0.43}_{-0.38}$ does not change significantly. This characteristic agrees with the lower concentration for merging clusters (e.g. Dutton & Macciò 2014; Klypin et al. 2016; Ishiyama et al. 2021). The same result was reported in optically-selected clusters (Okabe et al. 2019).

3.6. Mis-centering effect from 2D WL analysis

Since the two-dimensional analysis can treat the central positions as a free parameter, a distance between the eRASS1 cen-

Table 4. Parameters of the mis-centering effect.

	X-ray centroid	galaxy-peak
$\sigma_1 [h_{70}^{-1}\text{kpc}]$	$26.3^{+205.5}_{-24.8}$	$82.6^{+15.8}_{-17.4}$
$\sigma_2 [h_{70}^{-1}\text{kpc}]$	$218.2^{+47.2}_{-25.7}$	$347.5^{+28.2}_{-30.4}$
f_{cen}	$0.61^{+0.20}_{-0.10}$	$0.74^{+0.07}_{-0.07}$

troids and the WL-determined centers provides us with important information on the mis-centering effect. Since the S/N of the WL signals is not high enough (Figure 1), the centers and masses of some clusters are not well determined from the marginalized posterior distributions. If the WL-determined centers are associated with other clusters, we remove them from the results. The sample of the two-dimensional WL analysis using the spherical NFW model is limited to 36 clusters. The S/N of the lensing signal of the 36 clusters is $S/N \gtrsim 4$, with mean and median values of 5.4 and 5.1, respectively, belonging to a high S/N population in the parent samples (Sec 3.2).

Figure 10 shows the probability distribution of the best-fit distance from the eRASS1 centroids. The errors are estimated by randomly drawing from the posterior distributions. The distribution has a peak around $\sim 150 h_{70}^{-1}\text{kpc}$ and a tail at larger distances. To quantify the distribution, we introduce a model composed of two Gaussian components (Rayleigh distributions), as found in the previous studies (Oguri et al. 2010, 2018; Ota et al. 2023):

$$\frac{dP}{dr} = f_{\text{cen}}p_1(r) + (1 - f_{\text{cen}})p_2, \quad p_i(r) = \frac{r}{\sigma_i^2} \exp\left[-\frac{r^2}{2r\sigma_i^2}\right], \quad (22)$$

where f_{cen} is the fraction of the inner Gaussian and σ_i is a scale parameter (standard error). Since there are the measurement uncertainties of the WL-determined centers, we convolve the function (eq. 22) with the typical measurement error of $\sigma_{\text{err}} \approx 123 h_{70}^{-1}\text{kpc}$. The best-fit result is shown in Table 4. The scale parameters of the inner and outer components are at most $\sigma_1 \sim 26 h_{70}^{-1}\text{kpc}$ and $\sigma_2 \sim 218 h_{70}^{-1}\text{kpc}$, respectively.

Since there are multiple mass structures in some cluster fields, we also perform the multiple-component analysis. Compared to the result of the single NFW model, J141457.8-002050 and J141507.1-002905 (Figure 3) are added to the result. The probability distribution for the multiple-halo model is almost the same as that for the single-halo model (left panel of Figure 10). The probability distribution for the single elliptical NFW model is also similar to those for the single and multiple NFW models. The best-fits do not change. However, the errors for the two clusters become 10^3 times larger and the tail over $10^3 h_{70}^{-1}\text{kpc}$ is found (left panel of Figure 10). Therefore, the WL centers do not change significantly with a choice of mass models, and the mis-centering effect is small.

We also computed the probability distribution for the single NFW model centering the peaks in the galaxy maps, as shown in the right panel of Figure 10 and Table 4. The scale parameter of the inner component is about 3 times higher than that for the X-ray centroids. It shows that the X-ray centroids are a better tracer of the mass centers than the center of optical galaxies, thanks to the X-ray emissivity of n_e^2 .

3.7. Stacked mass map

Since the measurement of mis-centering effect by the 2D WL analysis is limited to clusters with high WL S/N (Sec 3.6), the effect is unclear for clusters with low WL S/N. We make stacked mass maps for the subsamples (Figure 11), centering

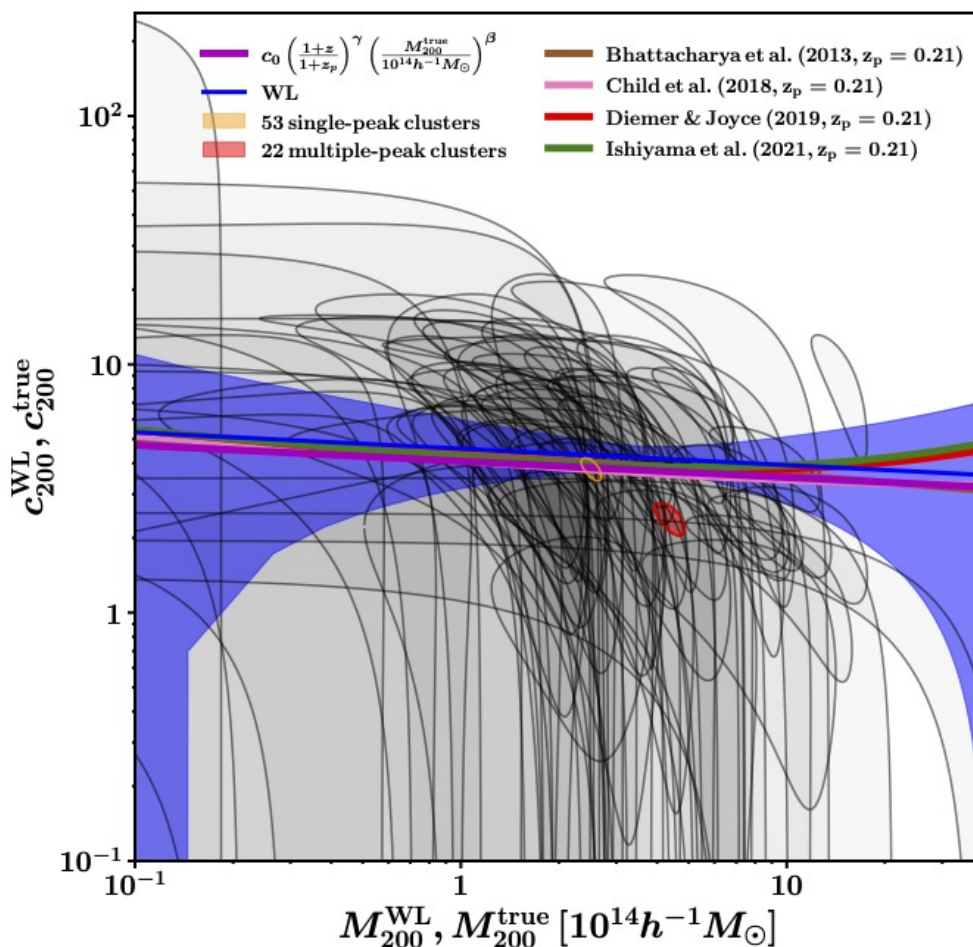


Fig. 8. The WL mass and concentration relation at $\Delta = 200$. The gray-shaded banana regions represent the 1σ constraint on mass and halo concentration for the 72 association clusters. The orange and red shaded regions represent the 1σ constraints by stacked lensing analysis for the 53 clusters with single galaxy peaks and the 22 clusters with multiple galaxy peaks, respectively. The best-fit line and its 1σ uncertainty are shown as the blue solid line and region, respectively. The magenta line is the best-fit for the true mass and the true concentration. The brown, pink, red, and green lines are the results of numerical simulations of [Bhattacharya et al. \(2013\)](#), [Child et al. \(2018\)](#), [Diemer & Joyce \(2019\)](#), and [Ishiyama et al. \(2021\)](#), respectively.

the eRASS1 X-ray centroids to visually investigate the mis-centering effect. The smoothing FWHM is 1 arcmin. The top three rows of Figure 11 show the S/N maps for different bins of richness, redshift, and S/N in the tangential shear profile, respectively. The subsamples do not include the poor-fit or mis-association clusters. The central region above 6σ has an almost concentric distribution. All of the peak centers coincide with the X-ray centroids within the smoothing scale. The average redshifts are about the same at ~ 0.2 , suggesting a similar lensing efficiency. The peak S/N increases with increasing richness and S/N, as expected from the mass-richness correlation in Sec. 3.4. The peak S/N in the redshift bins is highest at $0.2 \leq z < 0.4$, due to good lensing efficiency and a larger number of background galaxies. The peak SN for the poor-fit clusters has only a $\sim 3.6\sigma$ peak and no clear concentration. Even when we remove the sub-structure of the multiple-component cluster, J141457.8-002050 (Figure 3), the result does not change significantly. The SN map for the mis-association clusters shows no lensing signal.

We compare the peak S/N ($(S/N)_{\text{peak}}$) in the mass maps with the S/N in the stacked tangential shear ($(S/N)_{\langle\Delta\Sigma+\rangle}$) in the range

of $100\text{-}3000 h_{70}^{-1} \text{kpc}$. They are highly correlated for the S/N subsamples $\ln(S/N)_{\text{peak}} = 1.06 + 0.91 \ln(S/N)_{\langle\Delta\Sigma+\rangle}$. The subsample with $S/N < 4$, which could not be analyzed in the 2D WL, has a peak height similar to that expected from the S/N of the other two subsamples. Therefore, by analogy with the results of the 2D WL analysis of the other two samples, a subsample with $S/N < 4$ would have a similar level of mis-centering effect as the result of the 2D WL analysis.

The peak height is also weakly correlated with the cluster richness $\langle\lambda\rangle$; $\ln(S/N)_{\text{peak}} = 8.40 + 0.15 \ln\langle\lambda\rangle$. All the peaks expected from the richness are consistent with each other.

In contrast, the peak height of the poor-fit clusters is only 60 and 30 percent of those expected from $(S/N)_{\Delta\Sigma+} \simeq 4.1$ and $\langle\lambda\rangle \simeq 30$, respectively. Therefore, the mass distribution for the poor-fit clusters is completely different from the other 63 clusters.

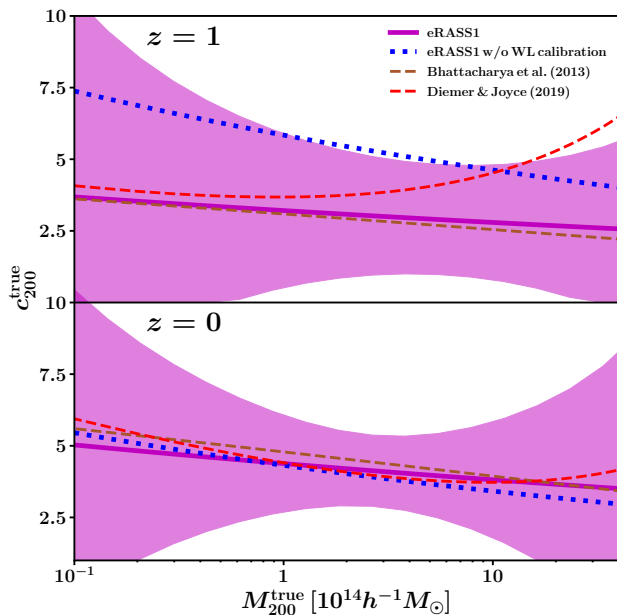


Fig. 9. Redshift evolution for the mass-concentration relation. The best-fit line and its 1σ uncertainty are shown as the magenta solid line and region, respectively. The blue dotted lines are the results without the WL calibration. The brown and red dashed lines denote the normalizations of numerical simulations of Bhattacharya et al. (2013) and Diemer & Joyce (2019), respectively.

3.8. Poor-fit clusters

3.8.1. WL mass measurements

Both the stacked tangential shear profile (Figure 6) and the stacked mass map (Figure 11) for the 12 poor-fit clusters have different characteristics from the other 63 association clusters. Here, the 12 poor-fit clusters are composed of 5 clusters including J141457.8-002050 (Figure 3) at $z < 0.2$, 5 clusters at $0.2 < z < 0.5$, and 2 clusters at $0.5 < z$, respectively. Since the lensing-weighted redshift is $\langle z \rangle = 0.19$, these average lensing properties are affected by the clusters at $z < 0.2$ because the number of background galaxies at $z > 0.4$ is much smaller than that at $z < 0.2$. Since the mass parameters of the subsamples split by redshifts are ill-constrained and their difference is not statistically significant, we examine the average characteristics for the poor-fit clusters.

When we fit the stacked tangential shear profile with a single NFW model, we obtain the extremely low concentration parameter of $c_{200} = 1.15^{+0.66}_{-0.47}$ (Figures 12 and 13). Indeed, the best-fit line is lower than the lensing signal observed in the central region of $r \lesssim 200 h_{70}^{-1} \text{kpc}$. To understand the discrepancy, we first add the point source at the center to the lensing model, but the best-fit point mass is too massive $\sim 3 \times 10^{13} h_{70}^{-1} M_{\odot}$ and the concentration parameter remains below 1. Since the lensing signals in the intermediate radius are low, the lensing profiles might be affected by the surrounding mass structures. Since the lensing signals for the poor-fit clusters are relatively low, we cannot identify the mass structure in the individual mass maps or find the eRASS1 clusters around the poor-fit clusters, except for J141457.8-002050 (Figure 3). Therefore, we instead use the galaxy maps as a proxy to compute the lensing signal from the surrounding halos. We fix the multi-halo positions and the best-fit WL masses for J141457.8-002050 obtained by 2D WL analy-

sis and the offset positions of the galaxy peaks. The surrounding halos are distributed over $0.2 - 1.9 h_{70}^{-1} \text{Mpc}$ for 6 clusters. The lensing-weighted average of the distance is $1.1 h_{70}^{-1} \text{Mpc}$. We parameterize the average mass associated with the galaxy peaks. Here, we assume that all the masses for the galaxy peaks are the same. Taking into account lensing weight in the stacked tangential shear profile, we compute the lensing signal from the surrounding halos as a function of M_{200} , where $c_{200} = 4$ or $c_{500} = 2.6$ is fixed. The modelled tangential shear profiles are computed by synthesizing the NFW mass model of the main cluster and the surrounding halos.

The constraints on the NFW parameters are weak, but not in contradiction with the baseline (left panel of Figure 13). The halo masses for the main cluster and its surroundings are $M_{200} = 0.31^{+0.24}_{-0.12} \times 10^{14} h_{70}^{-1} M_{\odot}$ and $M_{200}^{\text{sur}} = 4.07^{+2.12}_{-1.30} \times 10^{14} h_{70}^{-1} M_{\odot}$, respectively. Given the masses, we obtain $r_{200} \simeq 0.6 h_{70}^{-1} \text{Mpc}$ and $r_{200}^{\text{sur}} \simeq 1.4 h_{70}^{-1} \text{Mpc}$, respectively. Since the lensing-weighted average of the offset distances of the surrounding structures is $\sim 1.1 h_{70}^{-1} \text{Mpc}$, r_{200} slightly overlaps with each other. We re-run fitting for the 5 multi-halo clusters (excluding J141457.8-002050), and obtain $M_{200} = 0.19^{+0.16}_{-0.06} \times 10^{14} h_{70}^{-1} M_{\odot}$ and $M_{200}^{\text{sur}} = 2.68^{+0.83}_{-0.43} \times 10^{14} h_{70}^{-1} M_{\odot}$, respectively. The results do not change significantly. Since the surrounding halos are more massive than the eRASS1 clusters, the eRASS1 clusters are likely to be subhalos or halos accompanied by the surrounding halos. We note that the surrounding structures are not listed by the main eRASS1 X-ray catalogue (Merloni et al. 2024) except for J141457.8-002050.

As for the single-peak clusters, we obtain slightly higher mass $M_{200}^{\text{single}} = 0.53^{+0.33}_{-0.26} \times 10^{14} h_{70}^{-1} M_{\odot}$ and $c_{200}^{\text{single}} = 5.47^{+16.20}_{-5.46}$.

As mentioned above, the poor-fit clusters are less massive objects at $O(10^{13}) h_{70}^{-1} M_{\odot}$. They are broadly divided into two types with and without the surrounding mass structures. As for the clusters without the surrounding mass structures, the S/N in the stacked lensing profile is only 3.4. The WL mass measurements for these clusters are difficult simply because of the less massive objects. As for the clusters with the surrounding mass structures, the S/N in the stacked lensing profile is 9.4 but the lensing contamination from the surrounding structures cannot be ignored.

3.8.2. Scaling relations

We compute the stacked λ and the corrected CR for the 12 poor-fit clusters. The WL masses taken with and without the surrounding halos are shown by magenta squares and green triangles in Figure 13. In the mass-CR relation, the WL masses with and without the surroundings are $\sim 8\sigma_{\text{int}}$ and $\sim 4\sigma_{\text{int}}$ lower than those expected from the CR, respectively. Here, $\sigma_{\text{int}} = \sigma_{\text{CR}}/\beta_{\text{CR}}$ is the intrinsic scatter for the mass. Similarly, in the mass-richness relation, the WL masses with and without the surroundings are $\sim 7\sigma_{\text{int}}$ and $\sim 3\sigma_{\text{int}}$ lower, where $\sigma_{\text{int}} = \sigma_{\lambda}/\beta_{\lambda}$. These results are similar to the results of the stacked mass maps showing the different mass distribution (Sec. 3.7). Since the deviation of the mass from the mass-richness scaling relation is large, the galaxies in the surrounding structures might be counted in the richness. Therefore, it is important to distinguish clusters in such rich environments.

This result warns us that we need to take proper account of the surrounding mass structure for the less massive clusters in both the WL mass measurements and the richness measurement and, potentially, also, X-ray count-rate measurements.

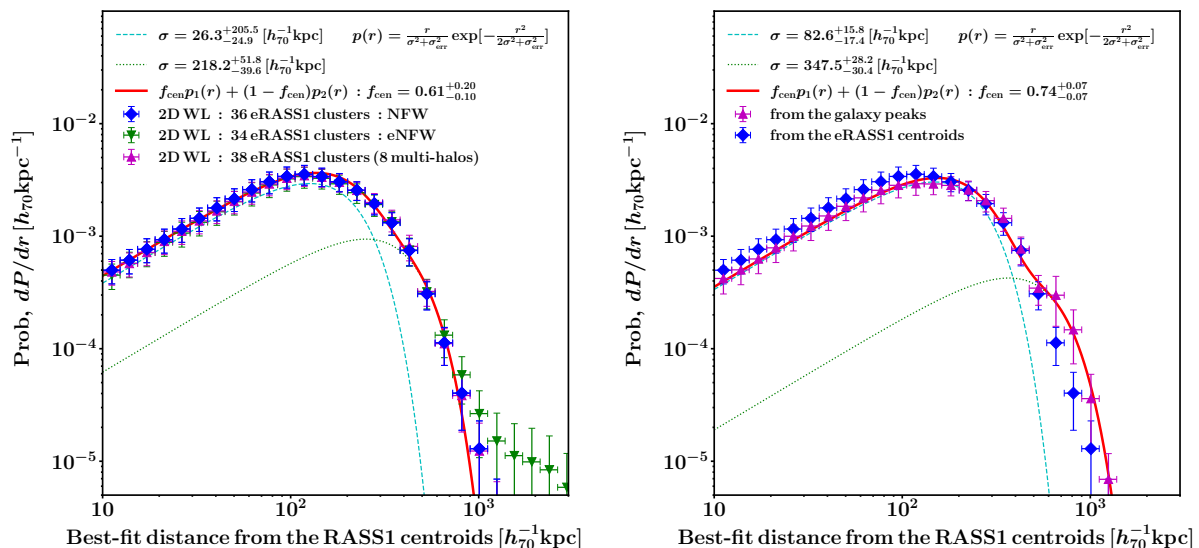


Fig. 10. *Left:* the best-fit distance from the eRASS1 centroids. The blue diamonds, green down-triangles, and magenta up-triangles represent the results of the spherical NFW model, the elliptical NFW model, and the inclusion of the multiple spherical NFW components, respectively. The red solid line, the light-blue dashed line, and the green dotted line are the best-fit for all the components, the inner Gaussian and the outer Gaussian, respectively. *Right:* The magenta up-triangles represent the distance from galaxy map peaks. The blue diamonds are the same as in the left panel.

3.9. 2D halo ellipticity

The probability distribution of the 2D halo ellipticity (ε) measured by the 2D WL analysis is shown in Figure 14. The number of clusters is 34. The errors are estimated by 50,000 Monte Carlo redistributions of the ellipticity parameter of each cluster. The average and median ellipticities are 0.45 and 0.47, respectively. The average measurement error for each cluster is 0.29. The probability distribution is slightly skewed; the probability at the lowest ellipticity bin is 1.4 times higher than that at the highest ellipticity bin. This is because we consider avoiding the zero bound by treating the absolute value but do not the bound at $\varepsilon = 1$. It is, therefore, difficult to conclude whether the skewed distribution is intrinsic or is due to the measurement technique. We fit the Gaussian distribution by convolving the average measurement error and obtain the mean ellipticity, 0.47, and the standard error 0.16.

We simultaneously obtain the orientation angle with a few percent measurement error. The small errors enable us to make a stacked mass map aligning the major axis with the y -axis (Figure 15), which gives a sanity check in our measurement. We adopt X-ray centroids as the center. Since the mis-centering effect is small, a choice of centers does not change the result. The 2D mass distribution is elongated along the y -axis, as expected by the 2D WL analysis. The degree and orientation angle of the elongation in the model-independent mass map are consistent with the result derived through the elliptical NFW model using discrete shear data. As a control sample, we make a stacked mass map with random orientations as shown in the top panel of Figure 15. The mass distribution is almost concentric, in contrast to the aligned mass map.

We stack eRASS1 soft-band (0.6–2.3 keV) images aligned with the major axis obtained by the 2D NFW fitting. We make X-ray images for individual clusters by subtracting the corresponding backgrounds and dividing them by the exposure maps. We here do not consider Galactic absorption at each cluster field because the clusters are located in a low Galactic column density region. We exclude X-ray images within 30 arcsec from X-

ray point-sources in the main eRASS1 X-ray catalogue (Merloni et al. 2024). The stacking weight is eq (16) to standardize the flux to its expectation at the average redshifts ($z_p = 0.19$) of the 34 clusters. The resulting map is shown in the top panel of Figure 16. We fit it with an elliptical β model; $S_X = S_0(1+(r/r_c)^2)^{-2\beta+0.5}$ where r is an iso-contour computed with the ellipticity (eq. 15) and obtain the ellipticity $\varepsilon_X \approx 0.1$. As expected, the best-fit major axis is aligned along the y axis. We stack the red galaxy maps, as shown in the bottom panel of Figure 16. We fit it with the elliptical β model added to a background component and obtain ellipticity $\varepsilon_G \approx 0.1$. When we use the galaxy map within 1 arcmin, the ellipticity becomes slightly higher $\varepsilon_G \approx 0.2$. The best-fit major axis is aligned with the y -axis. Thus, the ellipticities of the hot and cold baryonic components are smaller than that of the mass (mainly dark matter) component.

4. Discussion

4.1. Mass-richness-CR relation comparison

Fig. 7 shows the baselines of eRASS1 (red dotted line; Ghirardini et al. 2024), eRASS-DES (green dot-dashed line; Grandis et al. 2024) and eFEDS (orange dashed line; Chiu et al. 2022) clusters. The mass-dependent slopes for the CR and the richness, $\beta_{CR} = 1.310^{+0.294}_{-0.277}$ and $\beta_\lambda = 1.066^{+0.183}_{-0.216}$, are consistent with the slope in the soft-band X-ray luminosity and mass relation ($L_{\text{soft}}^X \propto M$) and the idea that the number of cluster members is proportional to the cluster masses. In contrast, our constraints on δ in the mass-dependent slope are poor due to the small number of our sample, while the literature (Chiu et al. 2022; Ghirardini et al. 2024; Grandis et al. 2024) constrains it well. We therefore compute the mass-dependent slopes in the literature (Chiu et al. 2022; Ghirardini et al. 2024; Grandis et al. 2024) at our lensing-weighted average redshift ($z_p = 0.21$) for the following comparison. Since the error covariance matrix of the regression parameters is not perfectly described in the literature, we simply use the best-fit baseline, which does not affect the following dis-

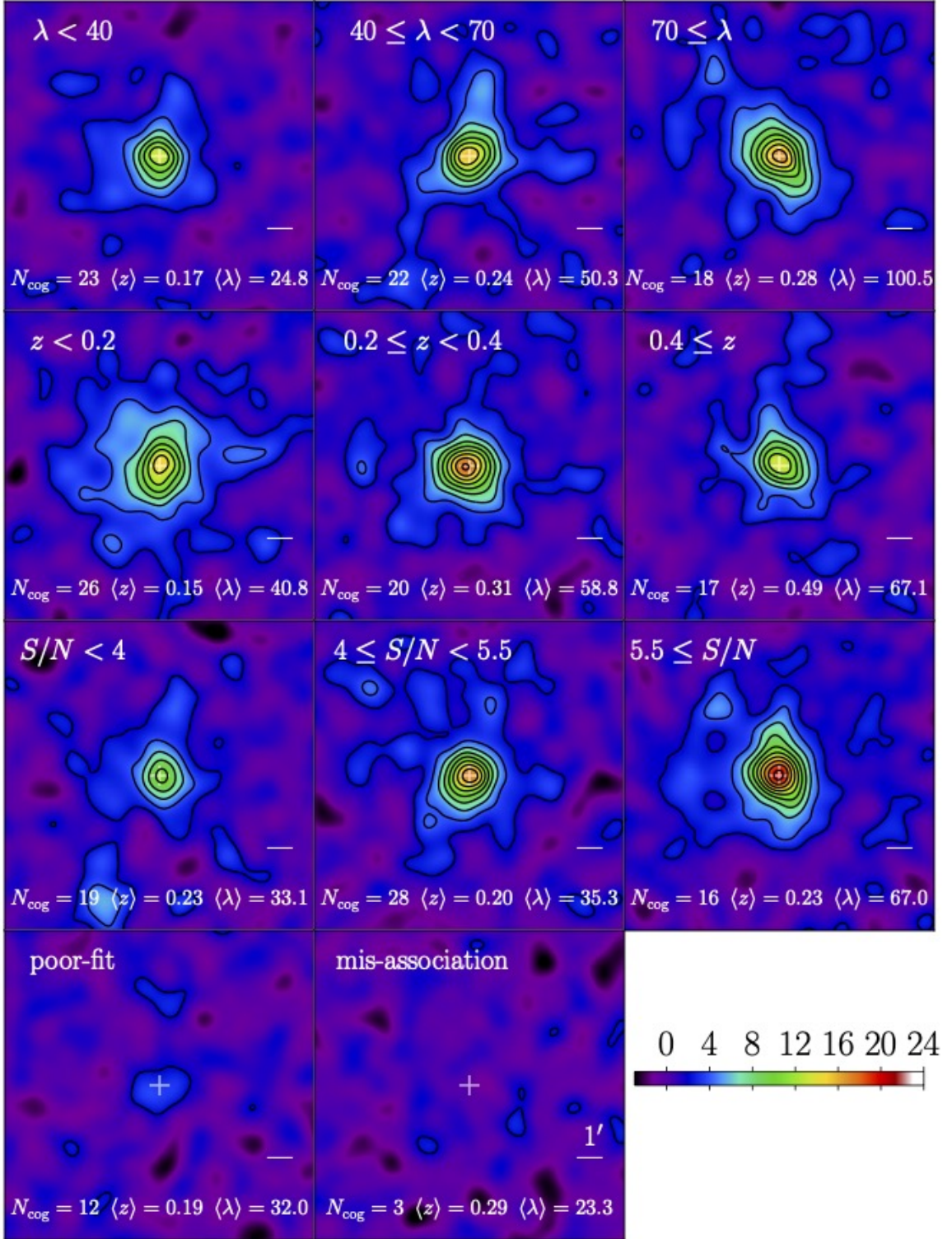


Fig. 11. The S/N of stacked mass maps for the subsamples ($12' \times 12'$). The black contours represent the reconstructed WL mass map spaced in units of 2σ bootstrapping error starting from 2σ . The first, second, and third rows from the top show the maps for the subsamples divided by richness, redshift, and the S/N in the tangential shear, respectively. These samples do not include the poor-fit nor mis-association clusters. The bottom panels show the mass maps for the poor-fit and mis-association clusters, respectively. The selection criteria are described in the upper part of each panel. The white crosses denote the eRASS1 centroids. The white horizontal line corresponds to the smoothing FWHM of $1'$. The number of clusters, the average redshift, and the average richness are described in the lower part of each panel.

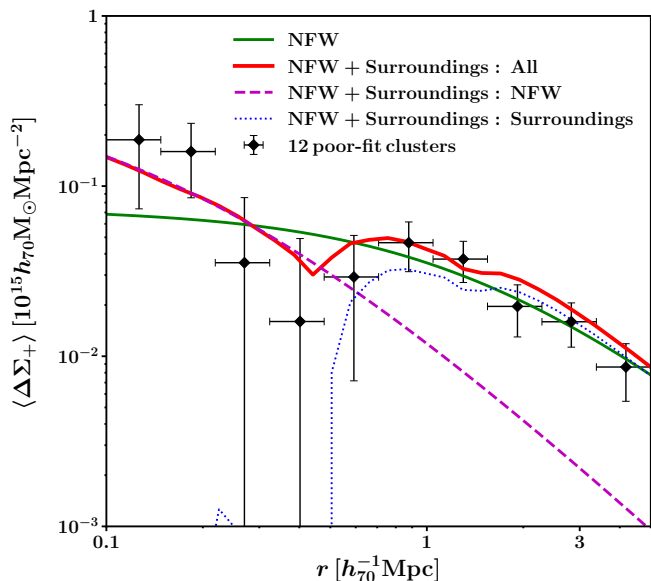


Fig. 12. Stacked tangential shear profile for the 12 poor-fit clusters (same as Figure 6). The green solid line denotes the best-fit model for a single NFW model, but showing $c_{200} = 1.16^{+0.68}_{-0.48}$. The red solid denotes the total lensing profile composed of the main NFW model and the surrounding halos. The magenta dashed and blue dotted lines are the tangential shear profiles of the NFW component and the surrounding halos, respectively.

discussion because our measurement errors are larger than those in the literature.

The best-fit slope of the mass-CR scaling relation is $1 \sim 2\sigma$ lower than $\beta_{\text{CR}} = 1.69$ (Chiu et al. 2022), $\beta_{\text{CR}} = 1.42$ (Ghirardini et al. 2024) and $\beta_{\text{CR}} = 1.71$ (Grandis et al. 2024). The intrinsic scatter of the count rate, $\sigma_{\text{CR}} = 0.344^{+0.097}_{-0.146}$, is comparable to the eFEDS-HSC result of $\sigma_{\text{CR}} = 0.301^{+0.089}_{-0.078}$ (Chiu et al. 2022), while $\sigma_{\text{CR}} = 0.98^{+0.05}_{-0.04}$ (Ghirardini et al. 2024) and $\sigma_{\text{CR}} = 0.61 \pm 0.19$ (Grandis et al. 2024) are more than twice as large as ours. Ghirardini et al. (2024) discussed very large intrinsic scatter by introducing the mass-dependent slope in intrinsic scatter and contamination of the active galactic nuclei and random sources and concluded that a further study is needed to understand the causes of very large intrinsic scatter. At least, we do not find such a large intrinsic scatter in the eFEDS-HSC and eRASS1-HSC analyses.

Our result of the mass and richness scaling relation agrees with the results of eRASS1 (Ghirardini et al. 2024) and eFEDS (Chiu et al. 2022), though the richness measurement of (Ghirardini et al. 2024) is different. Our mass-dependent slope agrees well with $\beta_{\lambda} = 0.98$ (Ghirardini et al. 2024) and $\beta_{\lambda} = 0.94$ (Chiu et al. 2022). The intrinsic scatter of the richness, $\sigma_{\lambda} = 0.350^{+0.099}_{-0.118}$, agrees well with $\sigma_{\lambda} = 0.274^{+0.078}_{-0.055}$ (Chiu et al. 2022) and $\sigma_{\lambda} = 0.32^{+0.04}_{-0.03}$ (Ghirardini et al. 2024).

4.2. Mis-centering effect

The results of the 2D WL analysis (Sec. 3.6) show that the probability distribution of the offset distance (Figure 10) is composed of the double peak structure. The standard error (scale parameter) of the inner component of the X-ray centroids is at most

$\sim 26 h_{70}^{-1} \text{kpc}$, which indicates that the X-ray centroids are a good tracer of the bottom of the gravitational potential projected on to the sky.

To confirm this result in an independent manner, we also fit the stacked lensing profile for the 36 clusters used in the 2D WL analysis and the 75 association clusters with the mis-centering NFW model. We choose X-ray centroids as the centers. Here we assume that the concentration parameter follows Diemer & Joyce (2019) and that the offset distances, d_{off} , are the same for all the clusters. In other words, the fitting procedure determines d_{off} to represent the concentration parameter (Diemer & Joyce 2019). We use the flat prior, $[\ln 0.02, \ln 0.5] h_{70}^{-1} \text{Mpc}$, for $\ln d_{\text{off}}$. We obtain $d_{\text{off}} = 46.2^{+20.7}_{-16.8} h_{70}^{-1} \text{kpc}$ and $38.0^{+18.4}_{-11.5} h_{70}^{-1} \text{kpc}$ for the 36 and 75 association clusters, respectively. They are consistent with the result obtained in the 2D WL analysis. Therefore, the mis-centering effect with the X-ray centroids is negligible on average when describing the lensing properties.

The scale parameter of the inner component using the galaxy peaks, $\sim 83 h_{70}^{-1} \text{kpc}$, is about 3 times larger than that using the X-ray centroids. In the stacked lensing analysis, we choose the innermost radius as $100 h_{70}^{-1} \text{kpc}$, the mis-centering effect would appear in the concentration parameter derived by the stacked lensing analysis. We repeat the stacked lensing analysis for the 36 clusters used in the 2D WL analysis using the galaxy peaks and obtain $c_{200}^{\text{WL}} = 3.02^{+0.31}_{-0.28}$ which is about $\sim 12.7\%$ lower than that using the eRASS1 centroids. The discrepancy is at the 1σ uncertainty level. In a similar way, we computed the stacked lensing profiles for 27 non-poor-fit clusters which could not be studied by the 2D WL analysis. The resulting concentration parameters using the galaxy peak centers and the eRASS1 centroids agree within the error. Hence, it is difficult to identify that the galaxy peaks are statistically more misaligned than the eRASS1 centroids for the less massive clusters.

We calculate the distance between galaxy peaks and the eRASS1 X-ray centroids. The resulting parameters of the 75 association clusters are $f_{\text{cen}} = 0.46^{+0.10}_{-0.10}$, $\sigma_1 = 43.4^{+6.2}_{-5.6} h_{70}^{-1} \text{kpc}$, and $\sigma_2 = 128.9^{+17.7}_{-12.5} h_{70}^{-1} \text{kpc}$. The resulting parameters of the 36 clusters used in the 2D WL analysis are similar to those for the 75 association clusters. Interestingly, the scale parameter of the inner component is smaller than that of the inner component between the WL-determined centers and galaxy peaks. In Figure 17, we compare the de-convolved separations between three different components. The X-ray centroids are the best tracer of the WL centers. The offset directions of the galaxy peaks from the eRASS1 centroids are different from those of the WL centers. As a result, the offset distance between the WL centers and the galaxy peaks is the largest.

Among the 12 poor-fit clusters, 6 clusters have surrounding halos. The average mass for the surrounding halos is more massive than that for the eRASS1 clusters (Sec. 3.8). Since these surrounding structures except for J141457.8-002050 are not identified by X-ray, it causes a possible source of mis-centering effect. We compute the probability distribution of the offset distance (Figure 10) including the 5 poor-fit clusters accompanied by the undetected surrounding structures, assuming that the true centers are in the surrounding halos and their uncertainty of the center determination is the mean value obtained by the 2D WL analysis. The scale parameters, σ_1 and σ_2 (eq. 22), change by only $\sim +5$ and $\sim +7\%$, respectively. Therefore, the mis-centering effect is statistically small in the whole sample.

Chiu et al. (2022) have computed the offset distribution between X-ray centroids and optical BCGs for the 313 eFEDS clusters and characterize it by a combination of a Rayleigh dis-

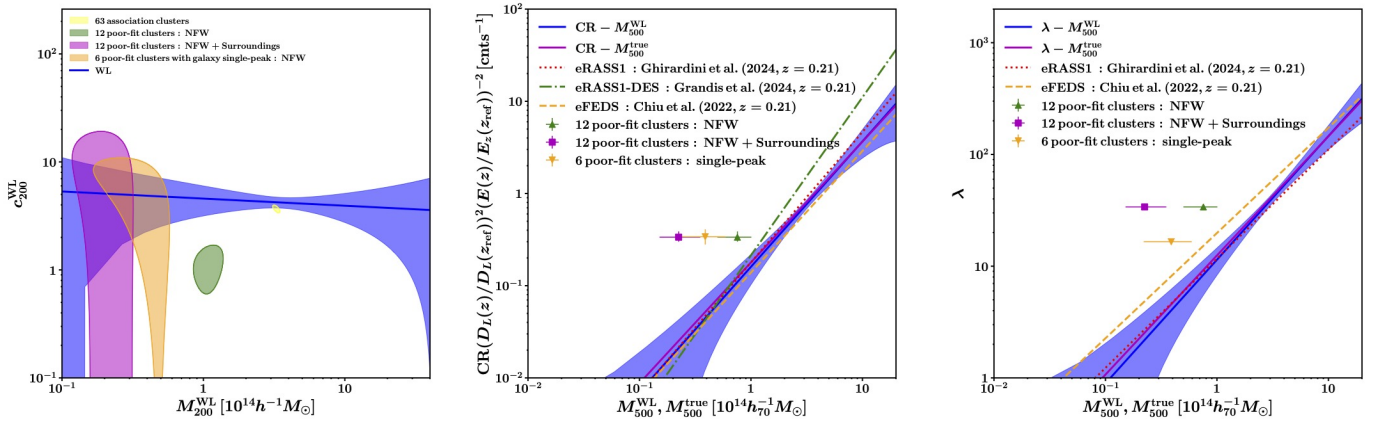


Fig. 13. Comparison of the baselines and the results of the poor-fit clusters. The green region and up-triangles are the results of the single NFW model for the 12 poor-fit clusters. The magenta region and squares are the results of the NFW component together with the surrounding mass halos in the model fitting. The orange region and down-triangles are the results of the single NFW model for the 6 poor-fit clusters with a single galaxy peak. *Left:* the mass-concentration relation. *Middle:* the mass and the corrected CR relation. *Right:* the mass and richness relation. The lensing contribution from the surrounding halos cannot be ignored for the poor-fit clusters. Once we consider the surrounding halos, the concentration agrees with the baseline, but the masses expected from the count-rate or the richness are significantly overestimated.

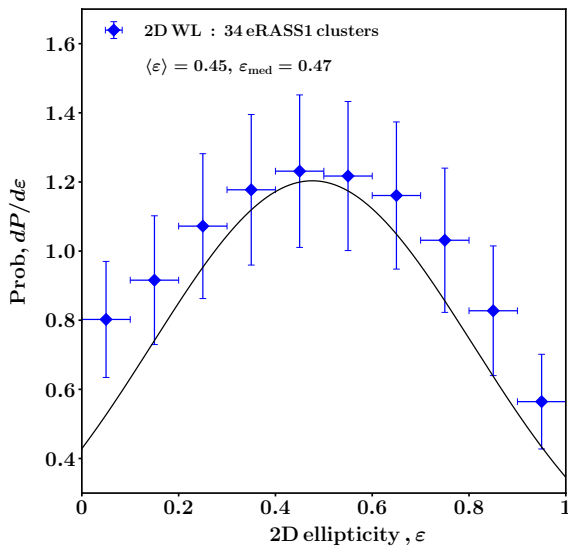


Fig. 14. The two-dimensional halo ellipticity distribution. The solid line is the best-fit Gaussian distribution convolved with the average measurement error.

tribution for the outer component and a modified Rayleigh distribution for the inner component. The best-fit scale parameters for the inner and outer components are $\sigma_1 = 0.17 \pm 0.01 h_{70}^{-1}$ Mpc and $\sigma_2 = 0.61 \pm 0.03 h_{70}^{-1}$ Mpc, and the fraction for the inner component is $f_{\text{cen}} = 1 - 0.54 \pm 0.02 = 0.46 \pm 0.02$. These parameters for the outer component are used as Gaussian priors for a simultaneous WL fit. The scale parameters are larger than our results between the galaxy peaks and the eRASS1 centroids. It might be due to the following feature that the galaxy peaks are insensitive to bright galaxies but sensitive to the number of member galaxies.

Grandis et al. (2024) have studied an intrinsic mis-centering using the hydrodynamical cosmological simulations. With 100 random viewing angles for the simulated 191 clusters (116 clusters at $z = 0.252$ and 75 clusters at $z = 0.518$), the offset be-

tween the peak of X-ray surface brightness distribution in 0.5–2 keV and the center-of-mass on the sky is well described by a single Rayleigh distribution with mean $\langle r_{\text{mis}}^{\text{int}} \rangle = \sigma_{\text{int}} r_{500}$ and $\sigma_{\text{int}} = 0.104 \pm 0.016$. Given the mean value, we obtain the scale parameter, $\sigma_1 = \langle r_{\text{mis}}^{\text{int}} \rangle (\pi/2)^{-1/2} \approx 0.082 r_{500}$ and $\sigma_1 \approx 80 h_{70}^{-1}$ kpc when we insert r_{500} for our sample. They also studied the observational mis-centering effect using the offset between input and output position of clusters in the "eROSITA all-sky survey twin" Seppi et al. (2022). Taking into account a realistic active galactic nucleus and cluster properties under the eRASS1 observational conditions, they obtained a typical mis-centering ~ 11 arcsec (see Sec. 4.2.2 in Grandis et al. 2024). They synthesized the two mis-centering effects in the WL mass measurement. Their mis-centering effect corresponds to our inner component.

Ota et al. (2023) have studied the offset distribution between X-ray centroids and NFW-determined centers by 2D WL analysis for the 23 HSC-CAMIRA clusters (Oguri et al. 2018) of which richness is higher than $N > 40$ in the eFEDS field. They obtained $\sigma_1 = 174 h_{70}^{-1}$ kpc, $\sigma_2 = 1339 h_{70}^{-1}$ kpc and $f_{\text{cen}} = 0.56$ for X-ray centroids of the CAMIRA clusters, where they did not consider the typical measurement errors for the WL centers. We refit it with the double-peak structure convolved with the typical measurement error of $\sigma_{\text{err}} = 170 h_{70}^{-1}$ kpc and obtain $f_{\text{cen}} = 0.56^{+0.05}_{-0.05}$, $\sigma_1 = 37.2^{+46.7}_{-30.4} h_{70}^{-1}$ kpc, and $\sigma_2 = 1328.5^{+111.3}_{-111.8} h_{70}^{-1}$ kpc. The scale parameter of the inner component is similar to ours. However, the scale parameter of the outer component is 7 times larger than ours. It might be caused by the fact that they did not check whether the WL-determined centers belong to other clusters. The scale parameters of the inner component from the CAMIRA centers and the galaxy peaks are $149.9^{+30.0}_{-32.0} h_{70}^{-1}$ kpc and $124.7^{+25.3}_{-26.5} h_{70}^{-1}$ kpc, respectively. Similarly, the central positions identified by galaxies are further away from the WL centers.

Melchior et al. (2017) carried out the WL mass calibration of redMaPPer clusters using the DES Science Verification field. They compared the centers of the redMaPPer clusters with X-ray data and SZ data from the South Pole Telescope. They considered the uncertainty of the X-ray and SZ centers (Rykoff et al. 2016) and found that the fraction of the central component is $f_{\text{cen}} = 0.76$ and the scale parameter is about 35% of the cluster radius determined by richness. Their results are similar to ours.

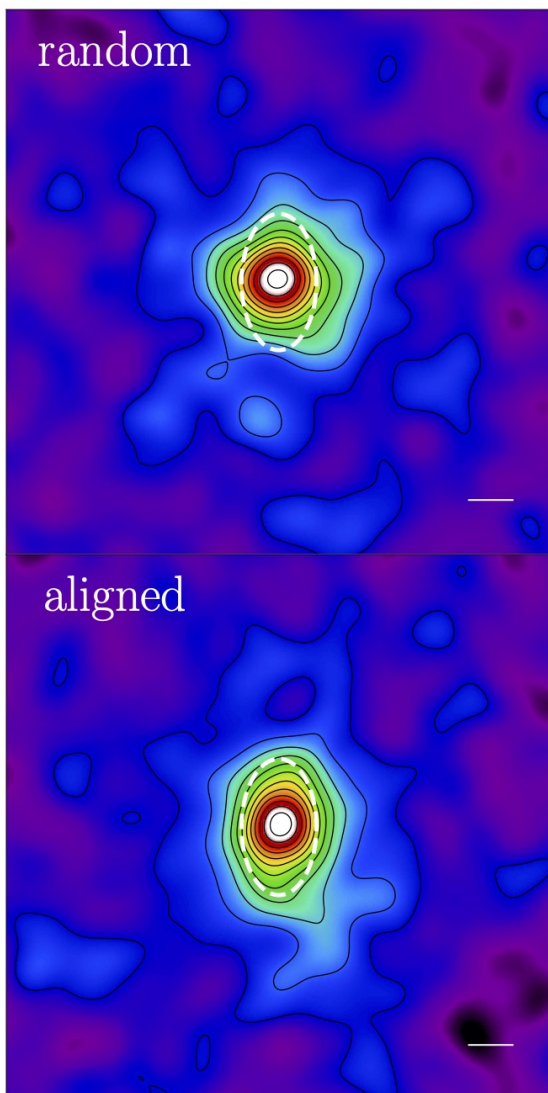


Fig. 15. The stacked mass maps for the 34 clusters analyzed with the elliptical NFW model. *Top*: random orientations. *Bottom*: aligned the major axis with the y -axis. The white dashed lines are an auxiliary line reflecting the median ellipticity. The white solid lines at the bottom right represent the 1 arcmin smoothing scale.

Bocquet et al. (2024) evaluated the mis-centering effect by combining the optical data of the DES and the Hubble Space Telescope and the SZ data from the South Pole Telescope. The central fractions for the SZ and optical distributions are 0.88 and 0.89. The scale parameters for the optical distribution are $\approx 10 h_{70}^{-1} \text{kpc}$ and $\approx 260 h_{70}^{-1} \text{kpc}$. The SZ distribution has similar properties. They also investigate the mis-centering effect using 70 clusters from *Chandra* X-ray data and found $f_{\text{cen}} = 0.8$, $\sigma_1 \approx 25 h_{70}^{-1} \text{kpc}$ and $\sigma_2 \approx 80 h_{70}^{-1} \text{kpc}$. Their results are similar to our findings from the 2D WL analysis.

4.3. Background selection

The main systematics of cluster mass measurements is a background selection. If cluster members are included in the shape

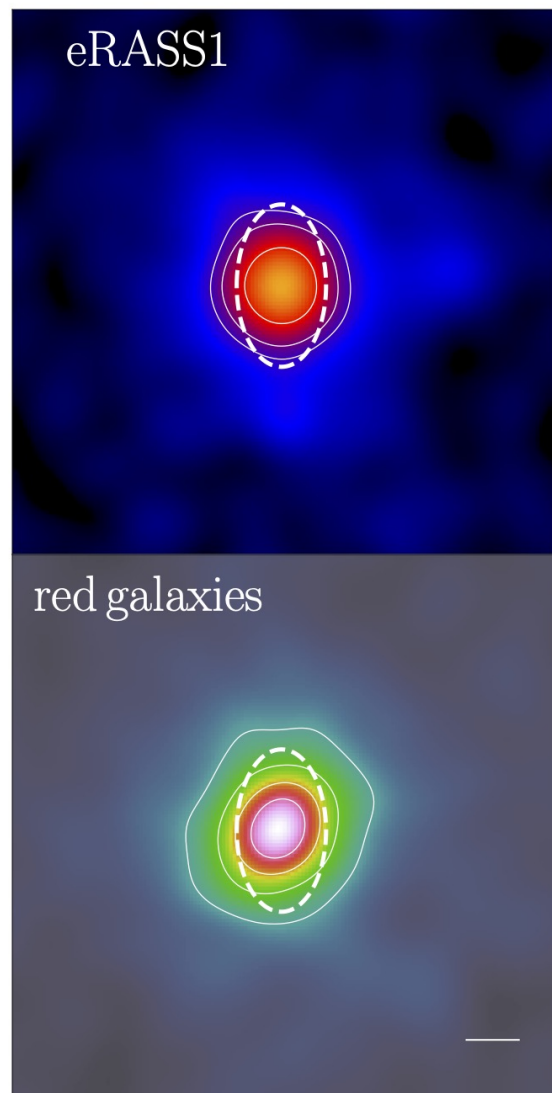


Fig. 16. The stacked eRASS1 (*Top*) and galaxy (*Bottom*) maps for the 34 clusters analyzed with the elliptical NFW model. The alignment is the same as Figure 15. The white dashed lines are an auxiliary line reflecting the median ellipticity. The white solid lines at the bottom right represent the one arcmin smoothing scale.

catalogue, the concentration parameter, c_{200} , or the masses, M_{Δ} ($\Delta \gtrsim 500$), within inner radii, are underestimated because the fraction of member galaxies to background galaxies increases with decreasing radius. The effect is known as a dilution effect (e.g. Broadhurst et al. 2005; Umetsu et al. 2014; Okabe & Smith 2016; Ziparo et al. 2016; Medezinski et al. 2018). Historically, the number of available imaging bands was limited, and background galaxies were selected in the colour-magnitude plane or the colour-colour plane (Umetsu et al. 2014; Okabe & Smith 2016), which is referred to as the colour-colour (CC) selection. The advantage of the CC selection is independent of the photometric redshifts. In the multi-band survey era, background galaxies can be selected using photometric redshifts, which is referred to as the P_z selection.

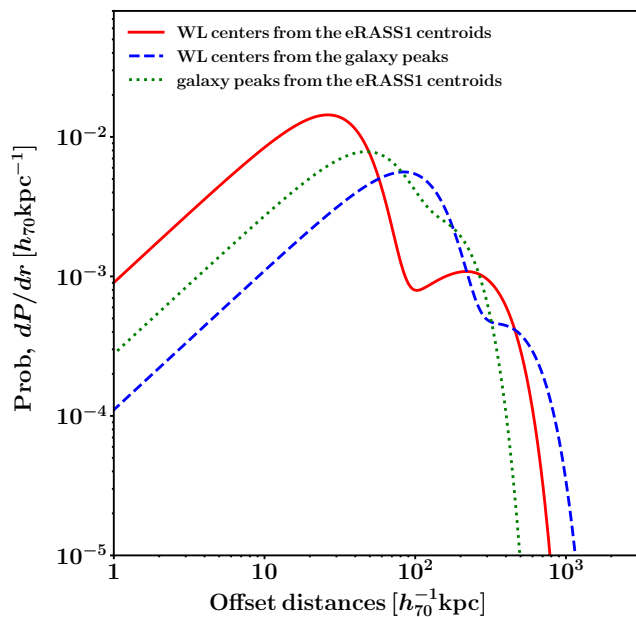


Fig. 17. Offset distances between the WL centers and the eRASS1 centroids (red solid line), between the WL centers and the galaxy peaks (blue dashed line), and between the galaxy peaks and the eRASS1 centroids (green dotted line). It indicates that the offset directions of the galaxy peaks are different from those of the WL centers.

Medezinski et al. (2018) have developed a new CC selection using the HSC five-band imaging through a monitor of colours and lensing signals. They also have found that the masses estimated with the CC and P_z selections are in good agreement. We repeat the same analysis using the CC selection as the P_z selection. A mass comparison is shown in Figure 18. We perform a regression analysis with $\ln M_{500}^{\text{WL,CC}} = \alpha_{\text{CC},P_z} + \beta_{\text{CC},P_z} \ln M_{500}^{\text{WL},P_z}$ and obtain $\alpha_{\text{CC},P_z} = 0.001^{+0.197}_{-0.228}$ and $\beta_{\text{CC},P_z} = 1.018^{+0.141}_{-0.121}$. The intrinsic scatter is < 0.138 . When we fix $\beta_{\text{CC},P_z} = 1$ and no intrinsic scatter, we obtain $\alpha_{\text{CC},P_z} = 0.030^{+0.077}_{-0.076}$, that is, the weighted geometric mean of the mass ratio of $1.030^{+0.081}_{-0.076}$. The masses of the two background selections are, therefore, in excellent agreement.

4.4. Mass-concentration relation

As discussed in Sec 4.2, the mis-centering effect is statistically negligible and thus does not affect the estimation of the halo concentration. The mass and concentration relation for the eRASS1 clusters agrees well with the numerical simulations as shown in Figure 8, which supports the assumptions of the mass-concentration relation adopted in the simultaneous WL mass measurements for the eRASS1 clusters (Chiu et al. 2022; Grandis et al. 2024; Kleinebreil et al. 2024).

Since the mass and concentration relation provides us with an opportunity to test hierarchical structure formation on a scale of Mpc, it has been well studied by various studies (Figure 19; e.g. Umetsu et al. 2014; Okabe & Smith 2016; Umetsu et al. 2016; Cibirka et al. 2017; Sereno et al. 2017; Okabe et al. 2019; Umetsu et al. 2020).

The cluster catalogue of the ROSAT All Sky Survey (RASS; e.g. Voges et al. 1999; Böhringer et al. 2004) were used for the WL analyses (Umetsu et al. 2014, 2016; Okabe & Smith 2016; Cibirka et al. 2017). The Subaru/Suprime-cam WL analy-

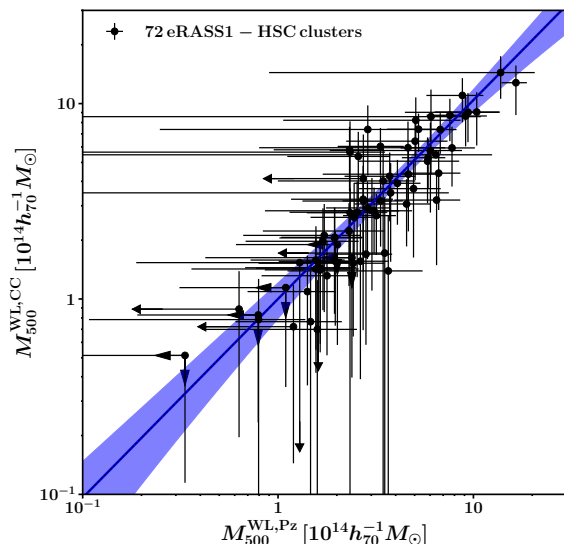


Fig. 18. A mass comparison with the P_z and CC selections. The blue solid line and the blue region are the best-fit and the 1σ uncertainty.

ses of CLASH (Umetsu et al. 2014, 2016) and LoCuSS (Okabe & Smith 2016) selected massive ROSAT clusters $M_{200} \gtrsim 5 \times 10^{14} h_{70}^{-1} M_{\odot}$ at a redshift slice $z \sim 0.2$. Since the number densities of background galaxies are more than twice that of our paper, they did not apply WL calibration. They found a negative mass-dependant slope but could not constrain the redshift evolution because of narrow redshift ranges. Cibirka et al. (2017) measured stacked mass and concentration for 27 massive clusters $M_{200} \sim 7 \times 10^{14} h_{70}^{-1} M_{\odot}$ at a redshift slice of $z \sim 0.5$ using the Canada-France-Hawaii Telescope (CFHT) data. Using the HSC-SSP shape catalogue, the XXL survey covers less massive clusters and groups of which masses cover down to $M_{200} \gtrsim 10^{13} h_{70}^{-1} M_{\odot}$ (Umetsu et al. 2020) in the wide redshift range of $0.031 \leq z \leq 1.033$. Our result agrees well with the mass-concentration relation for the RASS clusters (Umetsu et al. 2014, 2016; Okabe & Smith 2016; Cibirka et al. 2017) and the XXL clusters (Umetsu et al. 2020).

The concentration for the PSZ2 clusters from the *Planck* mission is somewhat lower than our concentration (Sereno et al. 2017).

As for optically-selected clusters, (Okabe et al. 2019) performed a stacked lensing analysis for the HSC-CAMIRA clusters (Oguri et al. 2018) to compare the concentration parameter for the single and multiple peaks in the galaxy maps. They did not consider the mis-centering effect in the mass modelling. The concentration parameter for the single-peak clusters is about 60% of the baseline. Since the mass measurement techniques are the same as our analysis, the mis-centering effect for the optically-selected clusters can not be ignored, as found in Ota et al. (2023) and Sec. 4.2. Okabe et al. (2019) have also shown that the halo concentration for the multiple-peak clusters is $\sim 33\%$ lower than that for the single-peak clusters. Similar results are found in our analysis; the ratio between the concentration parameters for the eRASS1 clusters with multiple-peak and single-peak is ~ 0.63 .

The cluster catalogue covering a wide redshift range enables us to measure the redshift evolution of normalization. (Umetsu et al. 2020) have shown the slope $\gamma = -0.03 \pm 0.47$. Our result gives similar result $\gamma = -0.449^{+1.152}_{-1.245}$. Since both measurement

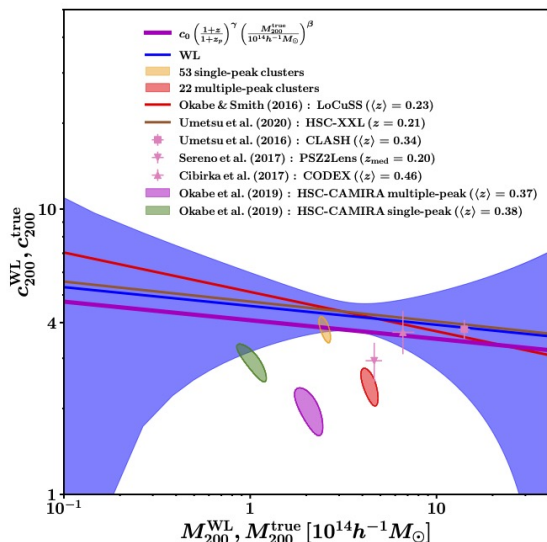


Fig. 19. A comparison with the literature. The blue solid line and the blue region are the best-fit and the 1σ uncertainty (Figure 8), respectively. The magenta line is the true mass and concentration relation. The red and brown lines are the best-fit lines of Okabe & Smith (2016) and Umetsu et al. (2020), respectively, where the redshift $z_{\text{ref}} = 0.3$ of Umetsu et al. (2020) is converted to $z = 0.21$. The orange and red shaded regions represent the 1σ constraints by stacked lensing analysis for the 53 clusters with single galaxy peak, and the 22 clusters with multiple galaxy peaks, respectively. The green and pink shaded regions represent the 1σ constraints by stacked lensing analysis for the HSC-CAMIRA clusters (Okabe et al. 2019) with single galaxy peak and multiple galaxy peaks, respectively. The pink square, up-triangle and down-triangle are the results of stacked lensing analyses of Umetsu et al. (2016), Cibirka et al. (2017) and Sereno et al. (2017), respectively.

errors are still large, we need a larger sample of clusters over wide redshift ranges.

As shown in Figure 8, the resulting baseline is in good agreement with dark-matter only numerical simulations (Bhattacharya et al. 2013; Child et al. 2018; Diemer & Joyce 2019; Ishiyama et al. 2021). Similar results have been reported in the literature (Umetsu et al. 2014, 2016; Okabe & Smith 2016; Cibirka et al. 2017). Child et al. (2018) have shown that the concentration parameter for the unrelaxed clusters is 69% of that for the relaxed clusters at $z = 0$. The feature is similar to our results. The redshift evolution is similar to the numerical simulations (Figure 9). However, the concentration parameters of different numerical simulations at $z = 1$ vary by up to $\gtrsim 50\%$ at the high mass end. To further constrain the redshift evolution in future studies, we need a large number of clusters at high redshifts and carefully treat the WL mass bias caused by a small number of background galaxies.

4.5. 2D halo ellipticity

We do not adopt any WL mass calibration in the halo ellipticity measurement. We leave this as next task using numerical simulations.

Our result agrees well with $\langle \varepsilon \rangle = 0.46 \pm 0.04$ of the pilot 2D WL study (Oguri et al. 2010). Umetsu et al. (2018) measured 2D halo ellipticity for 20 high-mass galaxy clusters selected from the CLASH survey and found $\langle \varepsilon \rangle = 0.33 \pm 0.07$ at $M_{\text{vir}} \approx 10^{15} M_{\odot}$. They discussed the CLASH selection func-

tion based on X-ray morphological regularity, with its average value being slightly lower than theoretical predictions. Chiu et al. (2018) constrained the minor-to-major axis ratio to mass scaling relation for the 20 CLASH clusters by a decomposition method using a strong and weak lensing dataset. Their result using the informative prior from dark matter simulations (Bonamigo et al. 2015) shows $\langle \varepsilon^{3D} \rangle \approx 0.50$ at a stacked WL mass $M_{200}^{\text{WL}} = 4.09^{+0.29}_{-0.27} \times 10^{14} h^{-1} M_{\odot}$ for the 34 clusters measured with the elliptical NFW model. Their result is similar to ours. The result provides us with constraints on the halo ellipticity in the mass range which is about half or less of the previous studies of $M_{200}^{\text{WL}} \sim 7 \times 10^{14} h^{-1} M_{\odot}$ (Oguri et al. 2010) and $M_{200}^{\text{WL}} \sim 10^{15} h^{-1} M_{\odot}$ (Umetsu et al. 2018; Chiu et al. 2018).

Although it is difficult to compare directly with 3D halo ellipticity, our results are similar to $\varepsilon \sim 0.45 - 0.55$ from numerical simulations (Despali et al. 2014; Bonamigo et al. 2015; Bett et al. 2007).

4.6. eRASS1 mass comparison

We compare individual WL masses with the eRASS1 masses (Bulbul et al. 2024). The eRASS1 masses are computed with the posterior distributions obtained by a simultaneous fit for the target cluster with priors of count-rate and mis-centering effect under an assumption of the mass and concentration relation (Chiu et al. 2022; Grandis et al. 2024; Kleinebreil et al. 2024). It is important to compare masses in a complementary way to our analysis.

The number of clusters for the comparison is 76 in total because the two mis-association clusters, J114647.4-012428 and J124503.8-002823, are listed in the cosmology sample (Ghirardini et al. 2024), but not in the primary sample (Bulbul et al. 2024). Among them, the masses of four clusters, including a mis-association cluster and two poor-fit clusters, are not listed in the primary sample, and our analysis cannot measure the WL masses for the two clusters. Thus, the number of samples is 70 clusters. Figure 20 shows a mass comparison, showing a good agreement. We perform the regression analysis with no redshift evolution of the normalization. The mass ratio between M_{500}^{eRASS1} and M_{500}^{true} is shown in the bottom panel of Figure 20. The baseline is consistent with unity within the 1σ level, though the best-fit value is -5% at $M_{500}^{\text{true}} = 10^{15} h_{70}^{-1} M_{\odot}$ and -5% at $10^{13} h_{70}^{-1} M_{\odot}$. As mentioned in Sec. 3.8, a treatment of surrounding halos at $0.2 - 1.9 h_{70}^{-1} \text{Mpc}$ from the poor-fit clusters of which masses are $O(10^{13} h_{70}^{-1} M_{\odot})$ is important. Even when we exclude the poor-fit clusters, the result do not change significantly. When we set the mass-dependent slope to unity, we obtain the ratio $0.937^{+0.067}_{-0.057}$ and $0.949^{+0.059}_{-0.053}$ for all the clusters and the sample excluding the poor-fit clusters, respectively.

5. Conclusions

We have presented individual WL mass measurements for 78 eRASS1 clusters in the HSC-SSP footprint. In the analysis, we do not adopt any priors for the eRASS1 X-ray quantities and the richness and the assumption of the mass and concentration relation, which is complementary to other WL mass measurements employed for the eFEDS or eRASS1 clusters (Chiu et al. 2022; Grandis et al. 2024; Kleinebreil et al. 2024).

The cluster sample is selected from the 103 eRASS1 clusters in the HSC-SSP footprint to provide a sufficient number of background galaxies, i.e., clusters where the background galaxies are not distributed over all azimuthal angles are removed. By

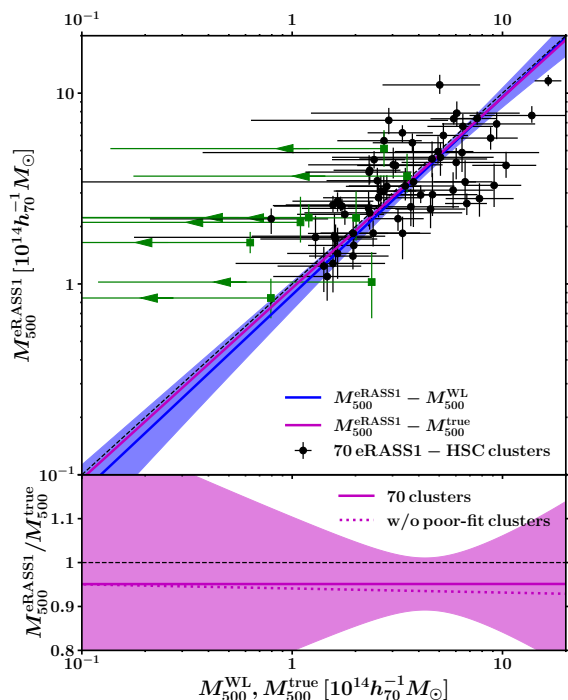


Fig. 20. *Top:* mass comparison between M_{500}^{WL} in this study and the eRASS1 mass in the primary sample (Bulbul et al. 2024). Black circles and green squares denote the association clusters the poor-fit clusters, respectively. The magenta and blue lines denote the best-fit $M_{500}^{\text{eRASS1}} - M_{500}^{\text{true}}$ and $M_{500}^{\text{eRASS1}} - M_{500}^{\text{WL}}$ relations, respectively. The blue region is the 1σ uncertainty of the baseline. *Bottom:* the ratio of M_{500}^{eRASS1} to M_{500}^{WL} . The magenta solid and dotted lines are the baseline for all the clusters and the 62 clusters excluding the poor-fit clusters, respectively. The magenta region is the 1σ uncertainty for all the clusters.

visual inspection of the HSC-SSP optical images, we have found that 3 out of the 78 eRASS1 clusters do not match with the optical counterparts (Figure 4). A null-lensing signal in its stacked lensing profile supports it (Figure 5).

Taking into account the WL mass calibration, the scaling relations between the true mass and cluster richness and X-ray count-rate agree well with the results of the eRASS1 Western Galactic Hemisphere region based on count-rate-inferred masses, which are calibrated with the HSC-SSP, DES, and KiDS surveys.

We developed a Bayesian framework to measure the true mass and concentration relation, taking into account the WL mass calibration in the mass and concentration plane. The redshift-dependent mass and concentration measurements are in excellent agreement with numerical simulations and previous studies.

Based on the 2D WL analysis, the offsets between the WL-determined centers and X-ray centroids for the 36 eRASS1 clusters with high WL S/N are described by two Gaussian components. The mis-centering effect with the X-ray centroids is small, as adopted in the previous studies (Chiu et al. 2022; Grandis et al. 2024). The stacked mass maps support it even for less massive clusters. In contrast, when we use the galaxy peaks, the mis-centering effect becomes slightly larger.

The projected halo ellipticity driven by the 2D WL analysis shows $\langle \varepsilon \rangle = 0.45$, which agrees with the results of numerical simulations and previous studies. The stacked mass map, aligned

with the major axes, represents the elongated structure obtained from the 2D WL analysis. The optical and X-ray ellipticities are $\varepsilon \approx 0.1 - 0.2$ and smaller than that of the dark matter distribution.

The average mass for the 12 poor-fit clusters changes from $\sim 10^{14} h_{70}^{-1} M_{\odot}$ to $\sim 2 \times 10^{13} h_{70}^{-1} M_{\odot}$ when lensing contamination from surrounding mass structures is taken into account. In that case, the concentration parameter is significantly improved from ~ 1 by including lensing contamination. For accurate WL mass measurement, modelling including surrounding halos or a choice of the maximum radius in the tangential shear profile is important.

Appendix A: Bayesian analysis for the mass-concentration relation

Taking into account the WL calibration on mass and concentration, the Bayesian framework for the mass and concentration analysis is slightly different from that for the multivariate scaling relations. To specify it, we summarize the formulation of the Bayesian analysis for the mass-concentration relation.

We introduce the logarithms of the true and actual WL mass and the true and actual WL concentration as follows: $X = \ln M_{200}^{\text{true}}$, $\tilde{x} = \ln \tilde{M}_{200}^{\text{WL}}$, $Y = \ln c_{200}^{\text{true}}$, $\tilde{y} = \ln \tilde{M}_{200}^{\text{WL}}$. We assume a linear regression between the true mass and the true concentration,

$$Y = \alpha + (\beta + \delta F(z))X + \gamma F(z) \quad (\text{A.1})$$

$$F(z) = \ln\left(\frac{1+z}{1+z_p}\right) \quad (\text{A.2})$$

where α , β , γ , δ are the normalization, the mass-dependent slope, the redshift-dependent slope in the normalization, and the redshift-dependent slope in the mass-dependent slope, respectively. The true concentration, Y_n , of the n -th cluster is randomly varied with the intrinsic scatter, $\sigma_Y(z_n) = \exp((\ln \sigma_Y)(1 + \gamma_{\sigma_Y} F(z_n)))$, from the baseline Y . Here, since the intrinsic scatter is a positive quantity, $\ln \sigma_Y$ is utilized as a parameter, and its redshift dependence is proportional to $\ln \sigma_Y$ to avoid negative values in σ_Y . The probability of Y_n given by X_n is written by

$$p(Y_n|X_n, \theta) = \mathcal{N}(\alpha + (\beta + \delta F(z_n))X_n + \gamma F(z_n), \sigma_Y(z_n)), \quad (\text{A.3})$$

where $\mathcal{N}(\mu, \sigma)$ is a Gaussian distribution with a mean, μ , and a standard error, σ , and θ is parameters in the mass and concentration relation composed of $\{\alpha, \beta, \gamma, \delta, \ln \sigma_Y, \gamma_{\sigma_Y}\}$, respectively. The parent population of X assumes a Gaussian distribution, $\mathcal{N}(\mu_X(z), \sigma_X(z))$, with a redshift-dependant hyper-parameters, $\psi = (\mu_X(z), \sigma_X(z))$. Here, $\psi(z) = \alpha_\psi + \sum_n \gamma_{\psi,n} F(z)^n$. The WL calibration between the true values and the actual WL values is described by

$$\begin{aligned} p(\tilde{\mathbf{x}}_n|\mathbf{X}_n) &= \mathcal{N}(\alpha'_{\text{WL}}(z_n) + \beta'_{\text{WL}}(z_n)\mathbf{X}_n, \Sigma_{\text{WL}}(z_n)), \\ \alpha'_{\text{WL}}(z) &= \alpha_{\text{WL}} + \gamma_{\text{WL}}F(z) \\ \beta'_{\text{WL}}(z) &= \beta_{\text{WL}} + \delta_{\text{WL}}F(z) \\ \Sigma_{\text{WL}}(z) &= \begin{pmatrix} \sigma_{\text{WL},x}^2(z) & r_{\text{WL},xy}(z)\sigma_{\text{WL},x}(z)\sigma_{\text{WL},y}(z) \\ r_{\text{WL},xy}(z)\sigma_{\text{WL},x}(z)\sigma_{\text{WL},y}(z) & \sigma_{\text{WL},y}^2(z) \end{pmatrix}, \\ \sigma_{\text{WL}}(z) &= \exp((\ln \sigma_{\text{WL}})(1 + \gamma_{\sigma_{\text{WL}}}F(z))) \\ r_{\text{WL},xy}(z) &= r_{\text{WL},xy}(1 + \gamma_{r_{\text{WL}}}F(z)) \end{aligned}$$

where $\tilde{\mathbf{x}}_n = (\tilde{x}_n, \tilde{y}_n)$, $\mathbf{X}_n = (X_n, Y_n)$, the WL mass calibrations (α_{WL} , β_{WL} , δ_{WL} , and γ_{WL}), and the intrinsic WL covariance Σ_{WL} , respectively. The observed WL mass and concentration, $\tilde{\mathbf{x}} = (\ln \tilde{M}_{200}^{\text{WL}}, \ln c_{200}^{\text{WL}})$, are related to the actual WL values with the error covariance matrix Σ_{err} , specified by

$$p(\mathbf{x}_n|\tilde{\mathbf{x}}_n) = \mathcal{N}(\tilde{\mathbf{x}}_n, \Sigma_{\text{err}}). \quad (\text{A.4})$$

The likelihood function is obtained by the Bayesian chain rule, as follows,

$$\begin{aligned} p(\mathbf{x}|\theta, \psi) & \\ \propto \prod_n \int d^2 \tilde{\mathbf{x}}_n \int d^2 \mathbf{X}_n p(\mathbf{x}_n|\tilde{\mathbf{x}}_n) p(\tilde{\mathbf{x}}_n|\mathbf{X}_n) p(Y_n|X_n, \theta) p(X_n|\psi), & (\text{A.5}) \end{aligned}$$

$$\propto \prod_n \frac{1}{2\pi \det(\Sigma_{\text{tot},n})^{1/2}} \exp\left[-\frac{1}{2} \mathbf{v}_n^T \Sigma_{\text{tot},n}^{-1} \mathbf{v}_n\right], \quad (\text{A.6})$$

Here, the vector, \mathbf{v} , and the total covariance matrix, Σ_{tot} , are given by

$$\mathbf{v} = \begin{pmatrix} x - (\alpha'_{\text{WL},x} + \beta'_{\text{WL},x}\mu_X) \\ y - (\alpha'_{\text{WL},y} + \beta'_{\text{WL},y}(\alpha' + \beta'\mu_X)) \end{pmatrix},$$

and

$$\alpha'(z) = \alpha + \gamma F(z) \quad (\text{A.7})$$

$$\beta'(z) = \beta + \delta F(z) \quad (\text{A.8})$$

$$\Sigma_{\text{tot}}(z) = \Sigma_{\text{err}} + \Sigma_{\text{int}}(z) + \Sigma_{\text{WL}}(z) + \Sigma_X(z), \quad (\text{A.9})$$

$$\Sigma_{\text{int}} = \begin{pmatrix} 0 & 0 \\ 0 & \beta_{\text{WL},y}^2 \sigma_Y^2 \end{pmatrix},$$

$$\Sigma_X = \begin{pmatrix} \beta_{\text{WL},x}^2 \sigma_X^2 & \beta' \beta'_{\text{WL},x} \beta'_{\text{WL},y} \sigma_X^2 \\ \beta' \beta'_{\text{WL},x} \beta'_{\text{WL},y} \sigma_X^2 & \beta'^2 \beta'^2_{\text{WL},y} \sigma_X^2 \end{pmatrix},$$

respectively.

Then, the posterior distribution is given by

$$p(\theta, \psi|\mathbf{x}) \propto p(\mathbf{x}|\theta, \psi) p(\theta) p(\psi). \quad (\text{A.10})$$

Here, $p(\theta)$ and $p(\psi)$ are priors. We adopt a flat prior $[-10^4, 10^4]$ to the normalization and a Student's t1 distribution with one degree of freedom on the slopes so that the slope angles become uniformly distributed. As for a non-informative prior distribution on the normalisation of the variance of the parent distribution, a scaled inverse χ^2 distribution as a conjugate prior, satisfying that posterior distributions have the same probability distribution family as the prior distribution.

Appendix B: WL mass calibrations

Cluster WL analysis extracts masses by an ensemble average of galaxy ellipticity which is composed of coherent WL signals synthesized to the intrinsic ellipticity. Thus, measurement accuracy depends on the number of background galaxies. For instance, there is no mass bias if an infinite number of background galaxies is available. In contrast, if the number of background galaxies was not sufficient, given the WL signal, each measured mass would be accidentally overestimated or underestimated. With the secure background selection using $P(z)$ in the HSC-SSP Survey, the number density of background galaxies depends strongly on the cluster redshift (Figures 2 and B.1), varying from ~ 10 to 1 [arcmin $^{-2}$] by changing the cluster redshift from 0.1 to 0.8. Even though we measure individual cluster masses, there might be bias and scatter in the measured WL masses.

We evaluate such systematics using a mock shape catalogue, realizing our observing conditions. We assume a spherical NFW model and no lensing effect from the large-scale structure. Other effects (e.g. mis-centering effect and halo triaxiality) as appeared in numerical simulations are not included. Although our tests include minimal effects, we placed more emphasis on a catalogue that represents the observational conditions and our analysis. To assess the bias and scatter in the WL mass measurement, the sufficient number of clusters in each mass and redshift bin is required, otherwise, an accidental over- or underestimation cannot be ruled out. The mock clusters are uniformly distributed in $[0.8, 30] h_70^{-1} 10^{14} M_\odot$ in a mass and $[0.1, 1]$ in a redshift. The concentration parameter uses [Bhattacharya et al. \(2013\)](#). The adopted number density of the background galaxies follows our result (bottom panel of Figure B.1). We randomly pick up galaxies from the all HSC catalogue ([Li et al. 2022](#);

Nishizawa et al. 2020), used in our analysis by satisfying eq. (1) as background galaxies. The catalogue contains the photometric redshift, its probability, and ellipticity. The spatial distributions of background galaxies are uniformly distributed, where we do not consider star mask effects. The intrinsic shape ellipticity is calculated by randomly rotating the catalogue ellipticity. We then synthesize the lensing signal to the intrinsic ellipticity. We make 9000 mock clusters and then repeat the same tangential shear analysis.

The upper panel of Figure B.1 shows a measurable fraction in the z and M_{200} plane. For a visual purpose, we smoothed it with a Gaussian kernel with $dz = 0.1$ and $\ln M_{200}^{\text{true}} = 0.35$. We successfully measure cluster WL masses at $z \lesssim 0.4$ and $M_{200} \gtrsim 5 \times 10^{14} h_{70}^{-1} M_{\odot}$ with more than 95%. In contrast, the higher the redshift and the lower the mass, the more difficult it is to measure WL masses. Therefore, our measured clusters selectively have a positive bias in the WL mass. The gray shadow region represents the z and M_{200}^{true} distribution for our sample of the eRASS1 clusters, obtained by the scaling relation analysis (Sec. 3.4). The sample is distributed around $\sim 95\%$ measurable fraction. Given the 75 association clusters, the number of the measurable clusters is $\sim 0.95 \times 75 \sim 71$, which agrees with our case of the 72 clusters.

There are two proposed WL mass calibrations. First is to calibrate between M_{500}^{WL} and M_{500}^{true} used in the scaling relations. The second is to calibrate the mass and concentration relation.

For the WL mass calibration of M_{500} , we use the x parameters only. Figure B.2 shows the mass bias (black circles), $M_{500}^{\text{WL}}/M_{500}$, for the mock clusters without the measurement errors and its average values (green boxes) in each mass and redshift bin. The measurable fraction (red solid lines) decreases as the mass is lower and the redshift is higher. Around the true mass where the measurable fraction is less than $\sim 50\%$, the black points are selectively deviated from the unity and its average values have positive biases. In contrast, the mass bias where the measurable fraction is more than $\sim 75\%$ is close to the unity. The mass dependence of the mass bias is likely to be non-linear. It is, therefore, necessary to reflect our mass distribution so that the WL mass calibration can be described by a linear equation. We first performed the scaling relation analysis without the WL mass calibration and measured the parent population. We then excluded the mass range where the probability of the target clusters being present is less than 10^{-6} . The excluded region where the mass bias varies non-linearly is represented by the magenta hatched boxes in Figure B.2. The resulting baseline parameters (blue solid lines in Figure B.2) are listed in Table B.1. The results do not change significantly if we adopt the minimum threshold of 10^{-5} or randomly select 90% sample of the clusters.

For M_{200}^{WL} and c_{200}^{WL} , we select the clusters with the condition that the probability of the target clusters being present is larger than 10^{-6} . The WL biases in M_{200} and c_{200} are correlated, as shown in Figure B.3. We evaluate the WL mass calibration parameters by simultaneously fitting all the measurements with the covariance error matrix. The result is shown in Table B.1. Since the intrinsic WL scatter in the mass and concentration is highly coupled, the intrinsic WL scatter becomes large.

In regression analysis, we use the parameters of the WL mass calibration as priors, taking into account its error covariance matrix.

Appendix C: Mass-richness-CR relation with $E(z)$

Since the redshift dependence of the overdensity masses follows $M_{\Delta} \propto \rho_{\text{cr}}(z)r_{\Delta}^3 \propto E(z)^{-1}$ and the soft-band luminosity follows

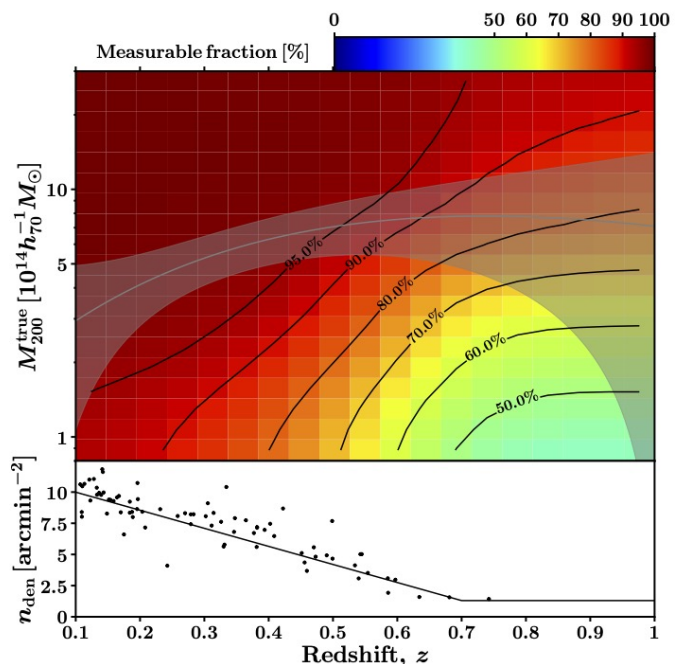


Fig. B.1. *Top:* the fraction of 3000 synthetic clusters for which WL masses can be measured in the M_{200}^{true} and z plane. The background colours are smoothed with a Gaussian kernel of $dz = 0.1$ and $d \ln M_{200}^{\text{true}} = 0.35$ for a visual purpose. The gray shadow region represents the true mass distribution obtained by a scaling relation analysis (Sec. 3.4). *Bottom:* the number densities as a function of cluster redshifts. The black solid line represents the model distribution used in the mock analysis.

Table B.1. WL mass calibrations for M_{200}^{WL} , c_{200}^{WL} and M_{500}^{WL} , where $\sigma_{\text{WL}} = \exp(\ln \sigma_{\text{WL}})$.

	$M_{200}^{\text{WL}}/c_{200}^{\text{WL}}$ [$10^{14} h_{70}^{-1} M_{\odot}$]	M_{500}^{WL} [$10^{14} h_{70}^{-1} M_{\odot}$]
M_p	$10^{14} h_{70}^{-1} M_{\odot}$	$10^{14} h_{70}^{-1} M_{\odot}$
c_p	4	-
$\alpha_{\text{WL},x}$	$0.110^{+0.021}_{-0.021}$	$0.079^{+0.024}_{-0.024}$
$\beta_{\text{WL},x}$	$0.933^{+0.009}_{-0.009}$	$0.965^{+0.011}_{-0.011}$
$\gamma_{\text{WL},x}$	$1.609^{+0.173}_{-0.174}$	$0.665^{+0.196}_{-0.198}$
$\delta_{\text{WL},x}$	$-0.375^{+0.041}_{-0.042}$	$-0.258^{+0.090}_{-0.090}$
$\alpha_{\text{WL},y}$	$0.108^{+0.017}_{-0.017}$	-
$\beta_{\text{WL},y}$	$0.947^{+0.028}_{-0.029}$	-
$\gamma_{\text{WL},y}$	$0.613^{+0.139}_{-0.141}$	-
$\delta_{\text{WL},y}$	$-0.586^{+0.120}_{-0.120}$	-
$\sigma_{\text{WL},x}$	$0.182^{+0.010}_{-0.010}$	$0.016^{+0.003}_{-0.003}$
$\gamma_{\sigma_{\text{WL},x}}$	$-0.619^{+0.200}_{-0.179}$	$-2.031^{+0.026}_{-0.025}$
$\sigma_{\text{WL},y}$	$0.319^{+0.011}_{-0.010}$	-
$\gamma_{\sigma_{\text{WL},y}}$	$-1.323^{+0.150}_{-0.146}$	-
r_{WL}	$-0.999^{+0.001}_{-0.000}$	-
$\gamma_{r_{\text{WL}}}$	0 (fixed)	-

$L_X \propto \rho_{\text{cr}}(z)^2 r_{\Delta}^3 \propto E(z)$, we here replace M_{500} , CR, and λ by $M_{500}E(z)$, $\text{CRE}(z)^{-1}$, and $\lambda E(z)$ in the scaling relation analysis, respectively. The result changes only the normalization in response to the replacement (the first column in Table C.1).

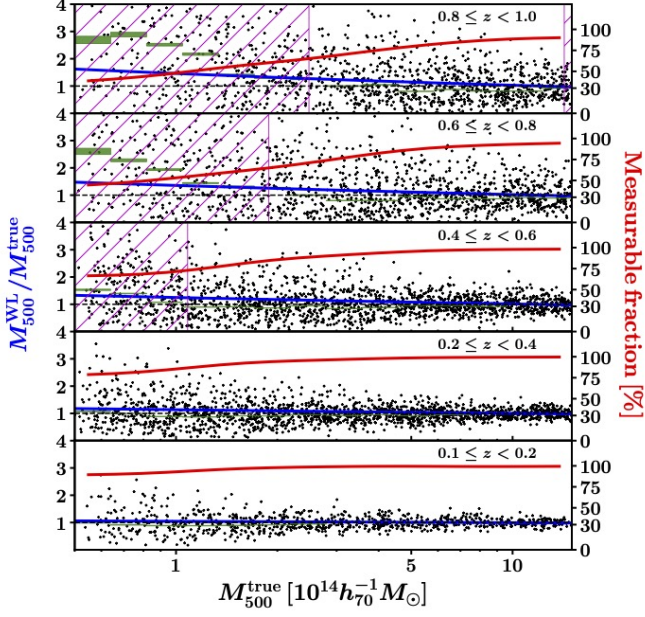


Fig. B.2. The mass bias, $M_{500}^{WL}/M_{500}^{true}$, in five redshift bins. The black points are the mass bias for individual mock clusters without their errors. The green patched regions are the averages in each mass bin. The red solid lines are the measurable fraction. The higher the redshift and the lower the mass, the more difficult it is to measure WL masses and the lower the measurable fraction. This leads to a selection mass bias in the measured quantities. The magenta hatched boxed are excluded regions in the mass bias fit, where the probability of the target clusters being present is less than 10^{-6} . The blue solid lines are the best-fit scaling relations for the mass bias.

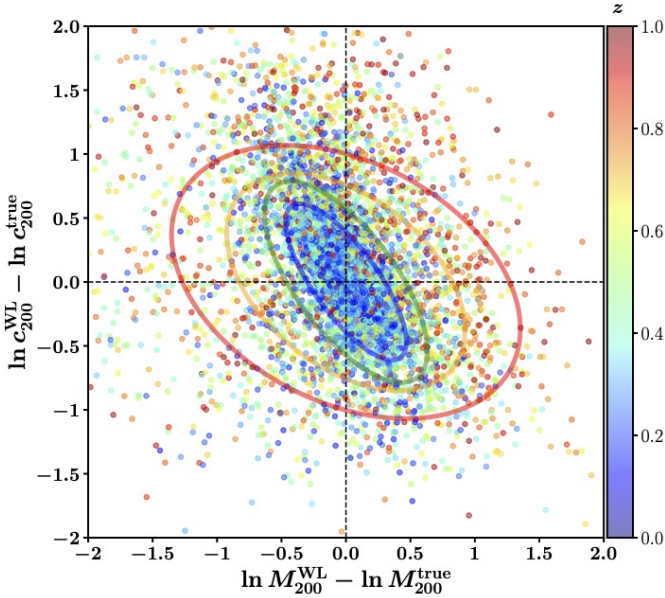


Fig. B.3. The points represent the logarithmic WL biases ($\ln M_{200}^{WL} - \ln M_{200}^{true}$ versus $\ln c_{200}^{WL} - \ln c_{200}^{true}$) for the sample with the presence probability that is higher than 10^{-6} . The colours denote redshifts. The elliptical lines in blue, green, orange, and red represent the covariance distribution composed of the intrinsic covariance and typical measurement errors at $z = 0.2, 0.4, 0.6,$ and 0.8 , respectively.

Table C.1. Scaling relation parameters using $M_{500}E(z)$, $CRE(z)^{-1}$, and $\lambda E(z)$ or CAMIRA richness, N . The fixed parameters are the same as (4) in Table 2.

	$E(z)$	CAMIRA
α_{CR}	$-1.786^{+0.339}_{-0.575}$	$-1.350^{+0.336}_{-0.389}$
β_{CR}	$1.306^{+0.506}_{-0.292}$	$1.012^{+0.308}_{-0.265}$
γ_{CR}	$1.544^{+1.482}_{-2.817}$	$2.508^{+1.143}_{-1.539}$
δ_{CR}	0 (fixed)	0 (fixed)
α_{λ}	$-1.167^{+0.256}_{-0.362}$	$-1.109^{+0.207}_{-0.241}$
β_{λ}	$1.108^{+0.234}_{-0.184}$	$1.053^{+0.168}_{-0.161}$
γ_{λ}	$-0.753^{+0.967}_{-1.056}$	$-2.168^{+0.808}_{-0.916}$
δ_{λ}	0 (fixed)	0 (fixed)
σ_{CR}	$0.226^{+0.180}_{-0.164}$	$0.463^{+0.136}_{-0.134}$
σ_{λ}	$0.368^{+0.106}_{-0.140}$	$0.357^{+0.115}_{-0.196}$
$r_{CR,WL}$	0 (fixed)	0 (fixed)
$r_{\lambda,WL}$	0 (fixed)	0 (fixed)
$r_{CR,\lambda}$	$-0.299^{+0.518}_{-0.420}$	$-0.419^{+0.369}_{-0.344}$

Appendix D: Mass-richness-CR relation with the CAMIRA richness

We cross-match the HSC CAMIRA clusters (Oguri et al. 2018, Oguri et al. in prep.) with the eRASS1 clusters. We used the internal CAMIRA catalogue with the S21A version. The tolerances for the spatial and redshift differences are 4 arcmin and 0.1 in the cross-matching. The 68 clusters out of the 78 eRASS1 clusters are matched. We replace the richness, λ , by the CAMIRA richness N_{camira} in the scaling relation analysis. Since masses for two clusters are not measurable, the number of clusters is 66 in the scaling relation analysis. The resulting parameters are described in the second column in Table C.1. The result changes little except for the redshift-dependent slope in the richness.

Acknowledgements. The Hyper Suprime-Cam (HSC) collaboration includes the astronomical communities of Japan and Taiwan, and Princeton University. The HSC instrumentation and software were developed by the National Astronomical Observatory of Japan (NAOJ), the Kavli Institute for the Physics and Mathematics of the Universe (Kavli IPMU), the University of Tokyo, the High Energy Accelerator Research Organization (KEK), the Academia Sinica Institute for Astronomy and Astrophysics in Taiwan (ASIAA), and Princeton University. Funding was contributed by the FIRST program from the Japanese Cabinet Office, the Ministry of Education, Culture, Sports, Science and Technology (MEXT), the Japan Society for the Promotion of Science (JSPS), Japan Science and Technology Agency (JST), the Toray Science Foundation, NAOJ, Kavli IPMU, KEK, ASIAA, and Princeton University. This paper makes use of software developed for the Large Synoptic Survey Telescope. We thank the LSST Project for making their code available as free software at <http://dm.lsst.org>. This paper is based [in part] on data collected at the Subaru Telescope and retrieved from the HSC data archive system, which is operated by Subaru Telescope and Astronomy Data Center (ADC) at NAOJ. Data analysis was in part carried out with the cooperation of Center for Computational Astrophysics (CfCA), NAOJ. We are honored and grateful for the opportunity of observing the Universe from Maunakea, which has the cultural, historical and natural significance in Hawaii. The Pan-STARRS1 Surveys (PS1) and the PS1 public science archive have been made possible through contributions by the Institute for Astronomy, the University of Hawaii, the Pan-STARRS Project Office, the Max Planck Society and its participating institutes, the Max Planck Institute for Astronomy, Heidelberg, and the Max Planck Institute for Extraterrestrial Physics, Garching, The Johns Hopkins University, Durham University, the University of Edinburgh, the Queen's University Belfast, the Harvard-Smithsonian Center for Astrophysics, the Las Cumbres Observatory Global Telescope Network Incorporated, the National Central University of Taiwan, the Space Telescope Science Institute, the National Aeronautics and Space Administration under grant No. NNX08AR22G issued through the Planetary Science Division of the NASA Science Mission Directorate, the National Science Foundation grant No. AST-1238877, the University of Maryland, Eotvos Lorand University (ELTE), the Los Alamos National Laboratory, and the Gordon and Betty Moore Foundation. This work is based on data from eROSITA, the soft X-ray instrument aboard SRG, a joint Russian-German sci-

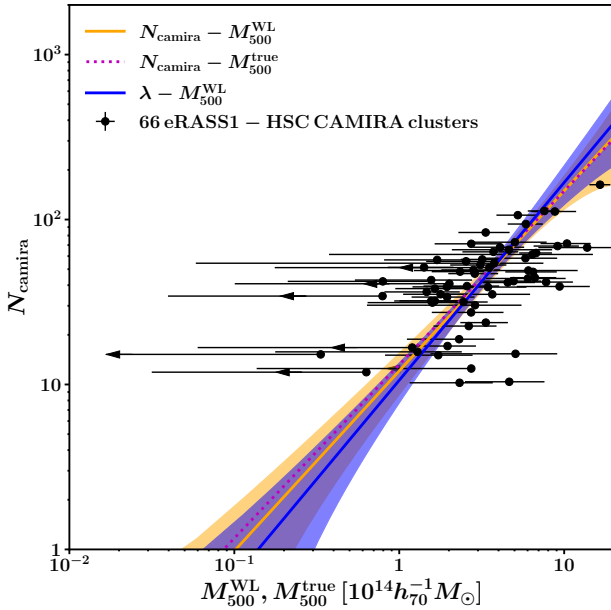


Fig. D.1. The CAMIRA richness and mass scaling relation. The black circles denote the overlapped 66 clusters. The orange solid and magenta dotted lines are the best-fit scaling relation with respect to the WL masses and the true masses, respectively. The orange region is the 1σ uncertainty of the scaling relation with the WL masses. The blue solid line and region are the best-fit and 1σ uncertainty with the eRASS1 richness (Figure 7), respectively.

ence mission supported by the Russian Space Agency (Roskosmos), in the interests of the Russian Academy of Sciences represented by its Space Research Institute (IKI), and the Deutsches Zentrum für Luft- und Raumfahrt (DLR). The SRG spacecraft was built by Lavochkin Association (NPOL) and its subcontractors, and is operated by NPOL with support from the Max Planck Institute for Extraterrestrial Physics (MPE). The development and construction of the eROSITA X-ray instrument was led by MPE, with contributions from the Dr. Karl Remis Observatory Bamberg & ECAP (FAU Erlangen-Nuernberg), the University of Hamburg Observatory, the Leibniz Institute for Astrophysics Potsdam (AIP), and the Institute for Astronomy and Astrophysics of the University of Tübingen, with the support of DLR and the Max Planck Society. The Argelander Institute for Astronomy of the University of Bonn and the Ludwig Maximilians Universität Munich also participated in the science preparation for eROSITA. N.O. and M.O. acknowledge JSPS KAKENHI Grant Number JP19KK0076. K.U. acknowledges support from the National Science and Technology Council of Taiwan (grant NSTC 112-2112-M-001-027-MY3) and the Academia Sinica Investigator Award (grant AS-IA-112-M04). E. Bulbul, A. Liu, V. Ghirardini, and X. Zhang acknowledge financial support from the European Research Council (ERC) Consolidator Grant under the European Union’s Horizon 2020 research and innovation program (grant agreement CoG DarkQuest No 101002585).

References

Abell, G. O. 1958, *ApJS*, 3, 211
Aguado, D. S., Ahumada, R., Almeida, A., et al. 2019, *ApJS*, 240, 23
Aihara, H., AlSayyad, Y., Ando, M., et al. 2022, *PASJ*, 74, 247
Aihara, H., Arimoto, N., Armstrong, R., et al. 2018, *PASJ*, 70, S4
Akino, D., Eckert, D., Okabe, N., et al. 2022, *PASJ*, 74, 175
Artis, E., Bulbul, E., Grandis, S., et al. 2024a, *arXiv e-prints*, arXiv:2410.09499
Artis, E., Ghirardini, V., Bulbul, E., et al. 2024b, *A&A*, 691, A301
Baldry, I. K., Liske, J., Brown, M. J. I., et al. 2018, *MNRAS*, 474, 3875
Bett, P., Eke, V., Frenk, C. S., et al. 2007, *MNRAS*, 376, 215
Bhattacharya, S., Habib, S., Heitmann, K., & Vikhlinin, A. 2013, *ApJ*, 766, 32
Bocquet, S., Grandis, S., Bleem, L. E., et al. 2024, *Phys. Rev. D*, 110, 083509
Böhringer, H., Schuecker, P., Guzzo, L., et al. 2004, *A&A*, 425, 367
Bonamigo, M., Despali, G., Limousin, M., et al. 2015, *MNRAS*, 449, 3171
Broadhurst, T., Takada, M., Umetsu, K., et al. 2005, *ApJ*, 619, L143

Bulbul, E., Chiu, I. N., Mohr, J. J., et al. 2019, *ApJ*, 871, 50
Bulbul, E., Liu, A., Kluge, M., et al. 2024, *A&A*, 685, A106
Bullock, J. S., Kolatt, T. S., Sigad, Y., et al. 2001, *MNRAS*, 321, 559
Carrasco Kind, M. & Brunner, R. J. 2014, *MNRAS*, 438, 3409
Child, H. L., Habib, S., Heitmann, K., et al. 2018, *ApJ*, 859, 55
Chiu, I. N., Ghirardini, V., Liu, A., et al. 2022, *A&A*, 661, A11
Chiu, I. N., Klein, M., Mohr, J., & Bocquet, S. 2023, *MNRAS*, 522, 1601
Chiu, I. N., Umetsu, K., Sereno, M., et al. 2018, *ApJ*, 860, 126
Chiu et al., I.-N. 2025, *arXiv e-prints*
Cibirka, N., Cypriano, E. S., Brimiouille, F., et al. 2017, *MNRAS*, 468, 1092
Clerc, N., Comparat, J., Seppi, R., et al. 2024, *A&A*, 687, A238
Colless, M., Peterson, B. A., Jackson, C., et al. 2003, *arXiv e-prints*, astro
Despali, G., Giocoli, C., & Tormen, G. 2014, *MNRAS*, 443, 3208
Diemer, B. & Joyce, M. 2019, *ApJ*, 871, 168
Diemer, B. & Kravtsov, A. V. 2015, *ApJ*, 799, 108
Dietrich, J. P., Erben, T., Lamer, G., et al. 2007, *A&A*, 470, 821
Dutton, A. A. & Macciò, A. V. 2014, *MNRAS*, 441, 3359
Gal, R. R., Lopes, P. A. A., de Carvalho, R. R., et al. 2009, *AJ*, 137, 2981
Ghirardini, V., Bulbul, E., Artis, E., et al. 2024, *A&A*, 689, A298
Goto, T., Sekiguchi, M., Nichol, R. C., et al. 2002, *AJ*, 123, 1807
Grandis, S., Ghirardini, V., Bocquet, S., et al. 2024, *A&A*, 687, A178
Heymans, C., Van Waerbeke, L., Bacon, D., et al. 2006, *MNRAS*, 368, 1323
Hilton, M., Sifón, C., Naess, S., et al. 2021, *ApJS*, 253, 3
Hirata, C. & Seljak, U. 2003, *MNRAS*, 343, 459
Ishiyama, T., Prada, F., Klypin, A. A., et al. 2021, *MNRAS*, 506, 4210
Kaiser, N. & Squires, G. 1993, *ApJ*, 404, 441
Klein, M., Oguri, M., Mohr, J. J., et al. 2022, *A&A*, 661, A4
Kleinebreil, F., Grandis, S., Schrabback, T., et al. 2024, *arXiv e-prints*, arXiv:2402.08456
Kluge, M., Comparat, J., Liu, A., et al. 2024, *A&A*, 688, A210
Klypin, A., Yepes, G., Gottlöber, S., Prada, F., & Heß, S. 2016, *MNRAS*, 457, 4340
Koester, B. P., McKay, T. A., Annis, J., et al. 2007, *ApJ*, 660, 239
Li, X., Miyatake, H., Luo, W., et al. 2022, *Publications of the Astronomical Society of Japan*, 74, 421
Lilly, S. J., Le Brun, V., Maier, C., et al. 2009, *ApJS*, 184, 218
Liu, A., Bulbul, E., Ghirardini, V., et al. 2022, *A&A*, 661, A2
Mandelbaum, R., Hirata, C. M., Seljak, U., et al. 2005, *MNRAS*, 361, 1287
Mandelbaum, R., Lanusse, F., Leauthaud, A., et al. 2017, *ArXiv e-prints* [arXiv:1710.00885]
Mandelbaum, R., Miyatake, H., Hamana, T., et al. 2018, *PASJ*, 70, S25
Mandelbaum, R., Rowe, B., Armstrong, R., et al. 2015, *MNRAS*, 450, 2963
Mandelbaum, R., Rowe, B., Bosch, J., et al. 2014, *ApJS*, 212, 5
Massey, R., Heymans, C., Bergé, J., et al. 2007, *MNRAS*, 376, 13
McCarthy, I. G., Schaye, J., Bird, S., & Le Brun, A. M. C. 2017, *MNRAS*, 465, 2936
Medezinski, E., Oguri, M., Nishizawa, A. J., et al. 2018, *PASJ*, 70, 30
Mehrtens, N., Romer, A. K., Hilton, M., et al. 2012, *MNRAS*, 423, 1024
Melchior, P., Gruen, D., McClintock, T., et al. 2017, *MNRAS*, 469, 4899
Merloni, A., Lamer, G., Liu, T., et al. 2024, *A&A*, 682, A34
Merloni, A., Predehl, P., Becker, W., et al. 2012, *arXiv e-prints*, arXiv:1209.3114
Miyaoka, K., Okabe, N., Kitaguchi, T., et al. 2018, *PASJ*, 70, S22
Navarro, J. F., Frenk, C. S., & White, S. D. M. 1996, *ApJ*, 462, 563
Navarro, J. F., Frenk, C. S., & White, S. D. M. 1997, *ApJ*, 490, 493
Nishizawa, A. J., Hsieh, B.-C., Tanaka, M., & Takata, T. 2020, *arXiv e-prints*, arXiv:2003.01511
Nishizawa, A. J., Oguri, M., Oogi, T., et al. 2018, *PASJ*, 70, S24
Oguri, M. 2021, *PASP*, 133, 074504
Oguri, M., Lin, Y.-T., Lin, S.-C., et al. 2018, *PASJ*, 70, S20
Oguri, M., Takada, M., Okabe, N., & Smith, G. P. 2010, *MNRAS*, 405, 2215
Okabe, N., Oguri, M., Akamatsu, H., et al. 2019, *PASJ*, 71, 79
Okabe, N. & Smith, G. P. 2016, *MNRAS*, 461, 3794
Okabe, N., Umetsu, K., Tamura, T., et al. 2016, *MNRAS*, 456, 4475
Okabe, N., Zhang, Y.-Y., Finoguenov, A., et al. 2010, *ApJ*, 721, 875
Ota, N., Nguyen-Dang, N. T., Mitsuishi, I., et al. 2023, *A&A*, 669, A110
Piffaretti, R., Arnaud, M., Pratt, G. W., Pointecouteau, E., & Melin, J. B. 2011, *A&A*, 534, A109
Popesso, P., Böhringer, H., Brinkmann, J., Voges, W., & York, D. G. 2004, *A&A*, 423, 449
Prada, F., Klypin, A. A., Cuesta, A. J., Betancort-Rijo, J. E., & Primack, J. 2012, *MNRAS*, 423, 3018
Predehl, P., Andritschke, R., Arefiev, V., et al. 2021, *A&A*, 647, A1
Reyes, R., Mandelbaum, R., Gunn, J. E., et al. 2012, *MNRAS*, 425, 2610
Rykoff, E. S., Rozo, E., Busha, M. T., et al. 2014, *ApJ*, 785, 104
Rykoff, E. S., Rozo, E., Hollowood, D., et al. 2016, *ApJS*, 224, 1
Scheider, P., van Waerbeke, L., Jain, B., & Kruse, G. 1998, *MNRAS*, 296, 873
Seppi, R., Comparat, J., Bulbul, E., et al. 2022, *A&A*, 665, A78
Sereno, M., Covone, G., Izzo, L., et al. 2017, *MNRAS*, 472, 1946
Sunyaev, R., Arefiev, V., Babyshkin, V., et al. 2021, *A&A*, 656, A132
Tanaka, M., Coupon, J., Hsieh, B.-C., et al. 2018, *PASJ*, 70, S9
Umetsu, K., Medezinski, E., Nonino, M., et al. 2014, *ApJ*, 795, 163
Umetsu, K., Sereno, M., Lieu, M., et al. 2020, *ApJ*, 890, 148
Umetsu, K., Sereno, M., Tam, S.-I., et al. 2018, *ApJ*, 860, 104
Umetsu, K., Zitrin, A., Gruen, D., et al. 2016, *ApJ*, 821, 116
Voges, W., Aschenbach, B., Boller, T., et al. 1999, *A&A*, 349, 389
Von Der Linden, A., Best, P. N., Kauffmann, G., & White, S. D. M. 2007, *MNRAS*, 379, 867
Wen, Z. L., Han, J. L., & Liu, F. S. 2009, *ApJS*, 183, 197
Ziparo, F., Smith, G. P., Okabe, N., et al. 2016, *MNRAS*, 463, 4004
Zwicky, F., Herzog, E., Wild, P., Karpowicz, M., & Kowal, C. T. 1961, *Catalogue of galaxies and of clusters of galaxies*, Vol. I

Affiliations

1. Physics Program, Graduate School of Advanced Science and Engineering, Hiroshima University, 1-3-1 Kagamiyama, Higashi-Hiroshima, Hiroshima 739-8526, Japan
2. Hiroshima Astrophysical Science Center, Hiroshima University, 1-3-1 Kagamiyama, Higashi-Hiroshima, Hiroshima 739-8526, Japan
3. Core Research for Energetic Universe, Hiroshima University, 1-3-1, Kagamiyama, Higashi-Hiroshima, Hiroshima 739-8526, Japan
4. Argelander-Institut für Astronomie (AIfA), Universität Bonn, Auf dem Hügel 71, 53121 Bonn, Germany
5. Universität Innsbruck, Institut für Astro- und Teilchenphysik, Technikerstr. 25/8, 6020 Innsbruck, Austria
6. Center for Frontier Science, Chiba University, 1-33 Yayoi-cho, Inage-ku, Chiba 263-8522, Japan
7. Department of Physics, Graduate School of Science, Chiba University, 1-33 Yayoi-Cho, Inage-Ku, Chiba 263-8522, Japan
8. Institute of Astronomy and Astrophysics, Academia Sinica, P.O. Box 23-141, Taipei 10617, Taiwan
9. Max Planck Institute for Extraterrestrial Physics, Giessenbachstrasse 1, 85748 Garching, Germany
10. IRAP, Université de Toulouse, CNRS, UPS, CNES, Toulouse, France
11. Institute for Frontiers in Astronomy and Astrophysics, Beijing Normal University, Beijing 102206, China